

Bandgap optimization in locally resonant metamaterial plates: A comparative study of five lattice geometries for low-frequency wave attenuation

A.H.R. Ferreira¹, E.J.P. Miranda Jr.^{1,1,1}, J.M.C. Dos Santos¹, A.M. Goto¹

^a *University of Campinas, UNICAMP-FEM-DMC, Rua Mendeleyev, 200, CEP 13083-970, Campinas, SP, Brazil*

^b *Federal Institute of Maranhão, IFMA-PPGEM, CEP 65030-005, São Luís, MA, Brazil*

^c *Federal Institute of Maranhão, IFMA-EIB-DE, CEP 65010-030, São Luís, MA, Brazil*

^d *Vale Institute of Technology, ITV-MI, CEP 35400-000, Ouro Preto, MG, Brazil*

Abstract

The attenuation of low-frequency flexural waves (10 – 200)[Hz] represents a persistent challenge in structural engineering, requiring innovative solutions that balance efficiency, compactness, and weight constraints. This study presents the first systematic comparative analysis investigating the combined influence of lattice geometry and local resonator frequency on band gap formation in thin Kirchhoff-Love plates across five distinct periodic configurations. The primary objective is to establish quantitative design guidelines for optimal lattice-resonator arrangements in the critical low-frequency range for aerospace, automotive, and civil engineering applications.

A comprehensive framework combining semi-analytical Plane Wave Expansion (PWE) and Extended Plane Wave Expansion (EPWE) methods with Finite Element Method (FEM) validation systematically analyzes 15 resonator frequencies across square, rectangular, triangular, honeycomb, and kagomé lattice configu-

*Corresponding author. Tel.: +55 11 958509690

rations. The semi-analytical approach demonstrates computational efficiency improvements of two orders of magnitude over conventional FEM while maintaining accuracy within 5% of numerical predictions.

Quantitative analysis reveals distinct performance hierarchies: triangular lattices achieve 40% wider band gaps compared to square configurations and demonstrate superior broadband characteristics; kagomé lattices provide up to 15 [dB] enhanced attenuation at low frequencies through triple-resonator coupling; honeycomb configurations offer balanced dual-band gap performance with coexisting frequency regions. Finite plates consistently exhibit 40 – 50% bandwidth expansion beyond infinite domain predictions due to boundary-induced mode coupling effects.

The research establishes the first quantitative hierarchy of lattice performance and provides engineers with systematic design guidelines for metamaterial plate optimization. This framework advances the field by bridging theoretical band gap predictions with practical finite plate performance, establishing essential tools for next-generation lightweight vibration isolation systems requiring efficient frequency-targeted vibration control.

Keywords: Locally resonant metamaterial, Flexural waves, Band gaps, Lattice configurations, Semi analytical method, Frequency-dependent optimization, Low-frequency vibration control.

¹ 1. Introduction

² Low-frequency noise and vibration mitigation represents a fundamental chal-
³ lenge in modern engineering applications, particularly within civil, naval, au-
⁴ tomotive and aerospace systems [? ? ? ? ? ? ?]. Structures exposed to
⁵ mechanical waves in the 20 [Hz] to 200 [Hz] range—including aircraft fuselages,
⁶ vehicle cabins, industrial machinery, and building floors—frequently experience
⁷ unwanted resonances and excessive structural vibrations [? ?]. These phenom-
⁸ ena precipitate substantial economic and operational consequences: material

⁹ fatigue reduces component lifespans by 25-40% in aerospace applications, ex-
¹⁰ cessive vibrations decrease industrial machinery efficiency by up to 15%, and
¹¹ noise-induced comfort degradation costs the aviation industry approximately
¹² \$3.2 billion annually in passenger compensation and operational delays [? ?].

¹³ Traditional passive noise control approaches, such as mass-damping systems
¹⁴ or viscoelastic coatings, impose severe design penalties: typical solutions re-
¹⁵ quire 150-300% mass increases to achieve 20 [dB] attenuation in the 20-200
¹⁶ [Hz] range, rendering them impractical for weight-sensitive applications where
¹⁷ every kilogram costs \$10,000-15,000 per flight hour in commercial aviation. Fur-
¹⁸ thermore, conventional treatments occupy 40-60% additional structural volume,
¹⁹ compromising payload capacity and architectural design flexibility [? ? ? ?
²⁰]. Consequently, the development of advanced acoustic metamaterials with tai-
²¹ lored bandgap properties has emerged as a critical technological imperative for
²² achieving effective wave attenuation while maintaining compact, lightweight de-
²³ signs that preserve operational performance and economic viability.

²⁴ The conceptual foundations of wave propagation control in structured materi-
²⁵ als trace back to pioneering developments in photonics during the late 1980s.
²⁶ The seminal works of Yablonovitch and John in 1987 [? ?] introduced the
²⁷ revolutionary concept of photonic band gaps (PBGs) in periodic dielectric me-
²⁸ dia, establishing the theoretical framework for electromagnetic wave manipu-
²⁹ lation. This breakthrough catalyzed rapid theoretical and experimental ad-
³⁰ vances: Meade et al. [?] provided the first theoretical demonstration of
³¹ two-dimensional PBGs, while Villeneuve and Piché [?] analyzed band-gap
³² formation in square and hexagonal lattices. The consolidation of this progress
³³ culminated in the paper by Joannopoulos [?], which demonstrated controlled
³⁴ electromagnetic wave manipulation in photonic crystals with immediate practi-
³⁵ cal impact.

³⁶ Inspired by these photonic developments, the early 1990s witnessed the emer-
³⁷ gence of phononics as researchers began investigating analogous concepts for

38 mechanical wave control in elastic media. Sigalas and Economou [?] provided
39 the first definitive demonstration of elastic-wave band gaps in two-dimensional
40 periodic systems in 1992, followed by Kushwaha et al. [?], who developed the
41 foundational theoretical framework for acoustic band structures in periodic elas-
42 tic composites. These pioneering contributions established the principles that
43 would guide subsequent phononic crystal research [?].

44 Phononic crystals (PCs) emerged as artificial structures composed of periodic
45 arrangements of materials with contrasting mechanical properties, typically in-
46 volving inclusions embedded in a host matrix. This concept, formalized in
47 the late 1990s by Laude and collaborators [? ?], operates through Bragg
48 scattering mechanisms that restrict wave propagation within specific frequency
49 bands—termed band gaps—when the structural periodicity approaches half the
50 wavelength [? ?]. The theoretical foundation draws from classical works by
51 Floquet [?], Bloch [?], and Brillouin [?], later consolidated through compre-
52 hensive reviews [? ?].

53 Despite their effectiveness, PCs face a fundamental limitation for low-frequency
54 applications: Bragg’s condition $a = n\lambda/2$ necessitates large unit cells to atten-
55 uate low-frequency waves [?], challenging compact device design, particularly
56 for flexural [?] or elastic waves in complex media [?].

57 The paradigm shift toward subwavelength metamaterials began with Liu et al.’s
58 [?] groundbreaking proposal of Locally Resonant Sonic Crystals (LRSCs).
59 Unlike conventional PCs that rely on interference, LRSCs utilize internal res-
60 onances to form band gaps at subwavelength scales, enabling lattice constants
61 two orders of magnitude smaller than the acoustic wavelength while achieving
62 deep low-frequency attenuation in compact structures.

63 Subsequent research rapidly expanded and validated this concept across mul-
64 tiple domains. Wang et al. demonstrated subwavelength band gaps in 2D
65 soft-inclusion composites [?] and extended the concept to 1D harmonic os-
66 cillator systems, revealing that stiffness contrast governs attenuation depth [?]

67]. Hsu et al. [?] showed that Lamb wave band gaps in thin plates depend
68 strongly on inclusion radius and thickness, while Oudich and colleagues explored
69 waveguiding in curved and straight channels [?] and experimentally confirmed
70 complete out-of-plane Lamb wave band gaps in stubbed plates using Brillouin
71 spectroscopy and laser vibrometry [?].

72 The theoretical analysis of wave propagation in metamaterial plates has evolved
73 through significant contributions to classical plate theory. The Kirchhoff–Love
74 and Mindlin–Reissner theories—originally formulated by Kirchhoff [?], Love
75 [?], Mindlin [?], and Reissner [?]—provide the foundation for understand-
76 ing flexural wave propagation in thin and moderately thick plates. Advanced
77 numerical methods, including the Plane Wave Expansion (PWE) approach [?]
78 and its Extended version (EPWE) [? ?], enable accurate band structure
79 predictions in complex periodic systems.

80 Building upon these developments, Xiao et al. investigated flexural wave prop-
81 agation in thin plates with periodic spring–mass resonators using EPWE [?],
82 revealing the coexistence of Bragg-type and locally resonant gaps, as well as
83 wide pseudo-gaps dependent on resonator natural frequency. Their subsequent
84 work demonstrated that beam-like resonators periodically attached to plates
85 can induce low-frequency complete band gaps for flexural waves [?], with tun-
86 able resonator properties allowing significant control over band gap location and
87 width.

88 Recent advances have further refined our understanding of metamaterial plate
89 behavior. Miranda et al. analyzed multi-DOF resonator arrays using PWE
90 validated with finite element simulations (FEM) and experiments [?], reveal-
91 ing similar attenuation levels for square and triangular lattices, though square
92 configurations exhibited wider Bragg-type gaps. Their extension to thick plates
93 with spring–mass resonators, applying Mindlin–Reissner theory through com-
94 bined analytical, numerical, and experimental methods [?], confirmed simulta-
95 neous formation of locally resonant and Bragg-type band gaps, further validating

⁹⁶ LRSCs as robust platforms for vibration attenuation.

⁹⁷ The practical implementation of metamaterial concepts has yielded numerous
⁹⁸ engineering applications. Flexural wave control in thin plates, demonstrated by
⁹⁹ Lee and Ruzzene [?] and Yao et al. [?], has found significant relevance in
¹⁰⁰ aerospace and automotive industries. Metamaterial barriers for vibration and
¹⁰¹ acoustic isolation have advanced through studies like Zouari et al. [?], while
¹⁰² acoustic panels for architectural acoustics were developed by Wang et al. [?].
¹⁰³ The integration of multiple physical phenomena—including piezoelectric effects
¹⁰⁴ for active control [?] and adaptive metamaterials with embedded shunt circuits
¹⁰⁵ [?]—has opened new possibilities for smart, adaptive metamaterial systems.

¹⁰⁶ Advanced design strategies have further enhanced metamaterial performance.
¹⁰⁷ Fractal-based phononic structures, such as hierarchical porous designs by Lee
¹⁰⁸ and Jeon [?], demonstrated that multi-level geometries can open multiple and
¹⁰⁹ widened band gaps. Auxetic microstructured metamaterials have shown novel
¹¹⁰ wave-control mechanisms [?], while embedding multiple local resonators within
¹¹¹ unit cells has proven effective [?]. Divergent-shaped unit cells, such as star-
¹¹² shaped configurations [?], have demonstrated low-frequency, wide band-gap
¹¹³ behavior, with viscoelastic damping layers further broadening performance [?].

¹¹⁴ Recent investigations have explored the relationship between lattice geometry
¹¹⁵ and attenuation performance. Wang et al. [?] investigated sandwich plate
¹¹⁶ structures with periodically embedded plate-type resonators, demonstrating sig-
¹¹⁷ nificant sound transmission loss, while Yan et al. [?] employed geometry
¹¹⁸ optimization to design diverse lattice configurations for enhanced low-frequency
¹¹⁹ vibration attenuation. The influence of resonator design on band-gap formation
¹²⁰ has been extensively studied through impedance mismatch effects [?], modal
¹²¹ coupling influences, and multilayer resonator arrangements [?], revealing criti-
¹²² cal design parameters for attenuation performance.

¹²³ Building upon these extensive developments, this study addresses the challenge
¹²⁴ of low-frequency noise and vibration control by presenting the first systematic

125 comparative analysis of the elastic band structure of flexural waves in infinite pe-
126 riodic plates with five distinct lattice configurations. The research is motivated
127 by the critical need to quantify design trade-offs: while metamaterial solutions
128 can achieve 20-40 [dB] attenuation with only 5-15% mass penalties (compared
129 to 150-300% for conventional approaches), optimal lattice selection remains em-
130 pirical, leading to suboptimal performance and missed opportunities for weight
131 and cost savings potentially worth millions of dollars in large-scale applications.

132 The investigation examines single-degree-of-freedom (SDOF) local resonator sys-
133 tems (SR-SDOF) arranged in square, rectangular, and triangular lattices, as
134 well as multiple local resonator systems (MR-SDOF) in honeycomb and kagomé
135 lattices. These five geometries represent the fundamental design space for
136 2D lattice metamaterials: square and rectangular lattices establish the base-
137 line orthogonal configurations commonly employed in manufacturing; triangu-
138 lar lattices provide the highest symmetry achievable with single resonators per
139 unit cell; honeycomb configurations introduce the simplest dual-resonator ar-
140 chitecture with practical manufacturability; and kagomé lattices represent the
141 most complex multi-resonator arrangement feasible within standard fabrica-
142 tion constraints. This selection encompasses the full spectrum from simple
143 (manufacturing-friendly) to complex (performance-optimized) configurations, en-
144 abling systematic evaluation of the geometry-performance-complexity trade-offs
145 critical for engineering implementation.

146 The comprehensive analysis employs both semi-analytical methods (PWE and
147 EPWE) and numerical simulations (FEM), demonstrating computational effi-
148 ciency improvements of two orders of magnitude while establishing quantitative
149 performance hierarchies among lattice configurations. This work provides crit-
150 ical insights into the dual influence of lattice geometry and resonator tuning,
151 enabling data-driven design decisions that can reduce development time by 60-
152 80% compared to trial-and-error approaches, while ensuring optimal solutions
153 for specific application requirements in weight-sensitive and performance-critical
154 engineering systems.

This paper is structured as follows: Section ?? presents the PWE approach for periodic plates based on Kirchhoff-Love theory, detailing the mathematical formulation for five lattice types (square, rectangular, triangular, honeycomb, and kagomé) with spring-mass resonators, including the derivation of eigenvalue problems and dispersion relations. Section ?? analyzes structure bands for local resonance frequency values ranging from 30 [Hz] to 200 [Hz], systematically comparing band gap widths, attenuation depths, and frequency evolution across all lattice configurations, while identifying critical performance metrics such as the triangular lattice's superior broadband performance and the kagomé's exceptional low-frequency attenuation. Section ?? validates the semi-analytical predictions through finite element simulations of 10×10 unit cell plates under point force excitation, comparing receptance curves and transmission loss to demonstrate the correlation between infinite-domain band structures and finite-plate vibration attenuation. Conclusions are presented in Section ??, synthesizing the quantitative design guidelines and performance hierarchies discovered. ?? and ?? provide the complete matrix formulations for PWE and EPWE implementations, including reciprocal lattice vectors, Fourier coefficients, and computational algorithms for complex wave vector extraction. ?? presents a comprehensive framework for lattice selection in engineering applications, providing quantitative decision tables and application-specific design guidelines derived from the comparative analysis.

2. Formulating LRSC unit cell models

This section presents a comprehensive formulation for thin LRSC plates using semi-analytical PWE and EPWE methods, based on Kirchhoff-Love plate theory [?].

2.1. Theoretical foundations

LRSC plates are modeled using Kirchhoff-Love theory for thin plates ($h/a < 0.1$) with spring-mass resonators providing local resonance effects (Figure ??).

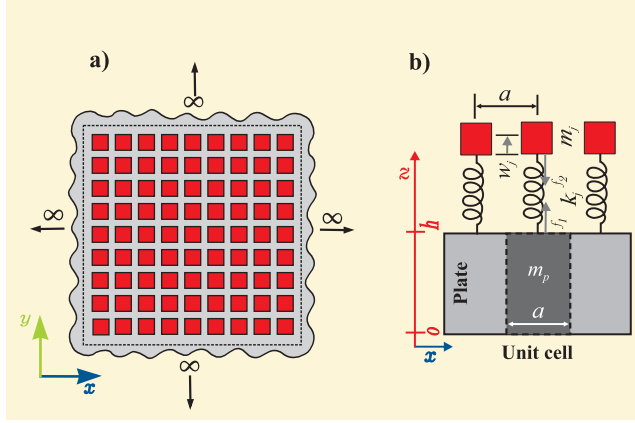


Figure 1: LRSC metamaterial configuration: (a) Infinite periodic array showing the global structure with spring-mass resonators (red squares) attached to the host plate. The dashed lines indicate the unit cell boundaries. (b) Detailed view of a single unit cell showing: plate mass m_p , resonator parameters ($m_{r,j}$, k_j , f_j), geometric dimensions (a , h), and coordinate system. The resonators provide local resonance at frequency $f_j = (2\pi^{-1})\sqrt{k_j/m_{r,j}}$.

183 This classical theory assumes plane sections remain plane and perpendicular
 184 to the neutral surface during bending, neglecting transverse shear deformation
 185 and rotatory inertia effects. The theory is valid when the plate thickness is
 186 much smaller than the characteristic wavelength, ensuring that flexural wave
 187 propagation is governed by the plate's bending stiffness rather than shear effects.
 188 The governing equation for flexural vibration with periodic resonator coupling
 189 is:

$$D\nabla^4 w(\mathbf{r}) - \omega^2 \rho h w(\mathbf{r}) = \sum_{j=1}^{N_j} \sum_{\mathbf{R}} p_j(\mathbf{r}_j + \mathbf{R}) \delta[\mathbf{r} - (\mathbf{r}_j + \mathbf{R})], \quad (1)$$

190 where $D = E^* h^3 / [12(1 - \nu^2)]$ is the complex bending stiffness with $E^* = E(1 +$
 191 $i\eta_p)$ being the complex Young's modulus incorporating plate damping through
 192 loss factor η_p , \mathbf{R} are lattice vectors defining the periodic repetition of unit cells,
 193 \mathbf{r}_j are the positions of resonators within a unit cell, and N_j resonators per unit

¹⁹⁴ cell. Resonator-plate coupling follows:

$$p_j(\mathbf{r}_j + \mathbf{R}) = k_j^*[u_j(\mathbf{r}_j + \mathbf{R}) - w(\mathbf{r}_j + \mathbf{R})], \quad (2)$$

¹⁹⁵

$$-\omega^2 m_{r,j} u_j(\mathbf{r}_j + \mathbf{R}) = -p_j(\mathbf{r}_j + \mathbf{R}), \quad (3)$$

¹⁹⁶ where $u_j(\mathbf{r}_j + \mathbf{R})$ is the displacement of the j th resonator mass and $w(\mathbf{r}_j + \mathbf{R})$
¹⁹⁷ is the flexural displacement of the plate at the resonator attachment point. The
¹⁹⁸ complex stiffness $k_j^* = k_j(1 + i\eta_j)$ incorporates the resonator damping effect.

¹⁹⁹ Eliminating the resonator displacement u_j from equations (??) and (??) yields
²⁰⁰ the resonator coupling force:

$$p_j(\mathbf{r}_j + \mathbf{R}) = \frac{-k_j^* \omega^2}{\omega^2 - \omega_{j,0}^2(1 + i\eta_j)} w(\mathbf{r}_j + \mathbf{R}) \quad (4)$$

²⁰¹ where $\omega_{j,0} = \sqrt{k_j/m_{r,j}}$ is the natural resonator frequency. Substituting this
²⁰² coupling into equation (??) and applying periodic Floquet-Bloch conditions
²⁰³ transforms the partial differential equation into a matrix eigenvalue problem
²⁰⁴ via reciprocal space expansion, as detailed in the following sections.

²⁰⁵ The plane wave truncation parameter M in the expansion $(2M+1)^2$ determines
²⁰⁶ the computational accuracy of the PWE method. Based on established practices
²⁰⁷ for similar phononic crystal analyses [? ?], this study employs $M = 5$ for
²⁰⁸ single-resonator and multi-resonator cases in the frequency range 10-200 [Hz]
²⁰⁹ with lattice parameter $a = 0.10$ m, ensuring wavelength resolution $\lambda/a > 5$ for
²¹⁰ adequate spatial discretization of the wave field.

²¹¹ *2.2. Semi-analytical methods overview*

²¹² This study employs two complementary semi-analytical approaches: Plane Wave
²¹³ Expansion (PWE) and Extended Plane Wave Expansion (EPWE). Table ??
²¹⁴ summarizes their key characteristics and applications.

Table 1: Comparison between PWE and EPWE methods for LRSC plate analysis.

Aspect	PWE Method	EPWE Method
Wave vector \mathbf{k}	Real values only	$\mathbf{k} \in \mathbb{C}, \mathbf{k} = \Re(\mathbf{k}) + i\Im(\mathbf{k})$
Evanescence modes	Ignored	Naturally incorporated
Primary application	Band structure calculation $\omega(\mathbf{k})$	Attenuation analysis $\mathbf{k}(\omega)$
Brillouin zone	Restricted to first zone	No restriction
Bandgap analysis	Identifies frequency ranges	Quantifies attenuation levels
Computational cost	Lower (eigenvalue problem)	Higher (generalized eigenvalue)
Physical insight	Propagating wave modes	Evanescence decay in bandgaps

²¹⁵ The combination of both methods provides complete bandgap characterization.

²¹⁶ PWE solves the forward eigenvalue problem:

$$[\mathbf{K} - \omega^2 \mathbf{M}] \boldsymbol{\phi} = 0, \quad \omega = \omega(\mathbf{k}) \quad (5)$$

²¹⁷ while EPWE solves the inverse problem for complex wave vectors:

$$[\mathbf{A}_3 k^3 + \mathbf{A}_2 k^2 + \mathbf{A}_1 k + \mathbf{A}_0] \boldsymbol{\psi} = 0, \quad k = k(\omega) \quad (6)$$

²¹⁸ The unit cell attenuation constant is defined as $\mu = \text{Im}\{k\} \cdot a$ [Np/cell], where
²¹⁹ Np denotes nepers (natural logarithm unit for attenuation: Attenuation [dB] =
²²⁰ $8.686 \times \mu$). With these analytical tools established, the following section examines
²²¹ how different lattice geometries influence the band structure formation and
²²² attenuation characteristics.

²²³ *2.3. Periodic lattice configurations*

²²⁴ Five lattice geometries with varying resonator configurations are analyzed: square
²²⁵ (1 resonator), rectangular (1), triangular (1), honeycomb (2), and kagomé (3).
²²⁶ These geometries span orthogonal to complex lattice symmetries, enabling comprehensive
²²⁷ bandgap performance evaluation.

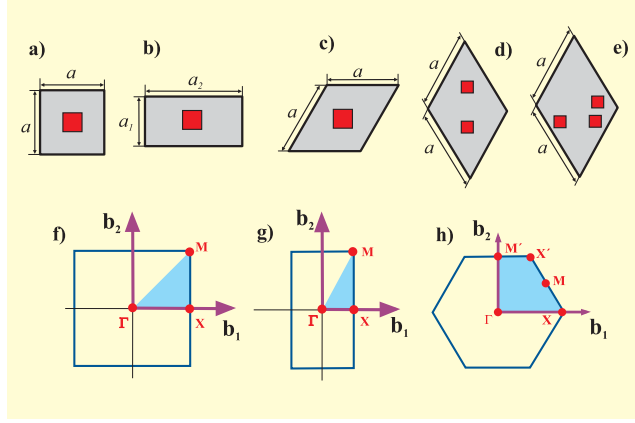


Figure 2: LRSC unit cells and FIBZ paths: (a) square, (b) rectangular, (c) triangular, (d) honeycomb, (e) kagomé lattices. Red squares: resonators. FIBZ high-symmetry paths: (f) Square/Rectangular: $\Gamma(0,0) \rightarrow X(\pi/a,0) \rightarrow M(\pi/a,\pi/a)$; (g) Triangular/Honeycomb/Kagomé: $M'(0,2\pi/3a) \rightarrow \Gamma(0,0) \rightarrow X(2\pi/3a,0) \rightarrow M(\pi/3a,\pi/\sqrt{3}a) \rightarrow X'(\pi/3a,\pi/\sqrt{3}a) \rightarrow M'$.

228 Primitive lattice vectors are: $\mathbf{a}_{1,2} = a\mathbf{e}_{1,2}$ (square), $\mathbf{a}_{1,2} = a_{x,y}\mathbf{e}_{1,2}$ (rectangular),
229 $\mathbf{a}_1 = a\mathbf{e}_1$ and $\mathbf{a}_2 = a(-\frac{1}{2}\mathbf{e}_1 + \frac{\sqrt{3}}{2}\mathbf{e}_2)$ (triangular), $\mathbf{a}_{1,2} = a\mathbf{e}_{1,2}$ (honeycomb), and
230 $\mathbf{a}_1 = a\sqrt{3}(\mathbf{e}_1 - \frac{1}{\sqrt{3}}\mathbf{e}_2)$ and $\mathbf{a}_2 = a\sqrt{3}(\mathbf{e}_1 + \frac{1}{\sqrt{3}}\mathbf{e}_2)$ (kagomé). Reciprocal lattice
231 vectors follow standard crystallographic relations $\mathbf{b}_i = 2\pi(\mathbf{a}_j \times \mathbf{e}_z) / (\mathbf{a}_i \cdot (\mathbf{a}_j \times \mathbf{e}_z))$.

232 2.4. PWE for thin LRSC unit cell thin plate configurations

233 PWE transforms the governing PDE into a matrix eigenvalue problem via
234 Fourier expansion in reciprocal space. The displacement field follows Floquet-
235 Bloch theorem:

$$w(\mathbf{r}) = e^{i\mathbf{k}\cdot\mathbf{r}} \sum_{\mathbf{G}} w(\mathbf{G}) e^{i\mathbf{G}\cdot\mathbf{r}} = \sum_{\mathbf{G}} w(\mathbf{G}) e^{i(\mathbf{k}+\mathbf{G})\cdot\mathbf{r}} \quad (7)$$

236 where reciprocal lattice vectors $\mathbf{G} = m\mathbf{b}_1 + n\mathbf{b}_2$ with integers $(m, n) \in [-M, M]$
237 and basis vectors $\mathbf{b}_i = (2\pi/S)(\mathbf{a}_j \times \mathbf{e}_z)$ for unit cell area S , consistent with the
238 $(2M+1)^2$ plane wave truncation used in computational implementation.

239 Resonator displacements satisfy:

$$w(\mathbf{r}_j) = \sum_{\mathbf{G}} w(\mathbf{G}) e^{i(\mathbf{k}+\mathbf{G})\cdot\mathbf{r}_j} \quad (8)$$

²⁴⁰ The eigenvalue problem formulation yields:

$$[\mathbf{K} - \omega^2 \mathbf{M}] \{\mathbf{q}\} = \mathbf{0} \quad (9)$$

²⁴¹ where \mathbf{K} and \mathbf{M} are stiffness and mass matrices, and $\mathbf{q} = [\mathbf{w}^T, \mathbf{u}^T]^T$ contains
²⁴² both plate wave amplitudes $\mathbf{w} = [w(\mathbf{G}_1), \dots, w(\mathbf{G}_{N_g})]^T$ and resonator displace-
²⁴³ ments $\mathbf{u} = [u_1, \dots, u_{N_j}]^T$. Matrix dimension is $[(2M+1)^2+N_j] \times [(2M+1)^2+N_j]$
²⁴⁴ with $N_g = (2M+1)^2$ plane waves and N_j resonators per unit cell. Complete
²⁴⁵ matrix assembly algorithms are detailed in ??.

²⁴⁶ The stiffness matrix \mathbf{K} from PWE contains fourth-order plate operators $|\mathbf{k} + \mathbf{G}|^4$
²⁴⁷ and resonator coupling terms that become frequency-dependent in EPWE. The
²⁴⁸ mass matrix \mathbf{M} contributions transform to complex dynamic stiffness expres-
²⁴⁹ sions $D_j(\omega)$ in the inverse formulation. This matrix relationship enables consis-
²⁵⁰ tent implementation of both forward $\omega(\mathbf{k})$ and inverse $\mathbf{k}(\omega)$ problems using the
²⁵¹ same physical parameters and geometric definitions.

²⁵² 2.5. EPWE for thin LRSC unit cell thin plate configurations

²⁵³ EPWE reformulates the eigenvalue problem to solve for complex wave vectors
²⁵⁴ $\mathbf{k}(\omega)$ at prescribed frequencies, enabling direct analysis of evanescent modes
²⁵⁵ and wave attenuation within bandgaps. The displacement field maintains the
²⁵⁶ Floquet-Bloch form:

$$w(\mathbf{r}) = e^{i\mathbf{k}\cdot\mathbf{r}} \sum_{\mathbf{G}} w(\mathbf{G}) e^{i\mathbf{G}\cdot\mathbf{r}}, \quad \mathbf{k} = k_r + ik_i \quad (10)$$

²⁵⁷ where the complex wave vector $\mathbf{k} \in \mathbb{C}$ allows for exponentially decaying modes
²⁵⁸ with attenuation constant k_i .

²⁵⁹ Resonator displacements follow the same expansion as Equation (??). Substi-
²⁶⁰ tution into the governing equation yields a polynomial eigenvalue problem:

$$[\mathbf{A}_3 k^3 + \mathbf{A}_2 k^2 + \mathbf{A}_1 k + \mathbf{A}_0] \psi = 0 \quad (11)$$

²⁶¹ where coefficient matrices \mathbf{A}_i contain lattice geometry and resonator coupling
²⁶² terms. The resonator dynamic stiffness incorporates frequency-dependent ef-

²⁶³ fects:

$$D_j(\omega) = k_j^* - \frac{(k_j^*)^2}{k_j^* - \omega^2 m_{r,j}} \quad (12)$$

²⁶⁴ Solution via companion matrix linearization provides complex eigenvalues $k =$
²⁶⁵ $k_r + ik_i$, where $\text{Im}\{k\} > 0$ quantifies evanescent decay. The unit cell attenu-
²⁶⁶ ation constant $\mu = \text{Im}\{k\} \cdot a$ [Np/cell] directly measures wave attenuation
²⁶⁷ within bandgaps. The polynomial eigenvalue problem is solved by transform-
²⁶⁸ ing Eq. (??) into a generalized linear eigenvalue problem of size $4N_g \times 4N_g$,
²⁶⁹ where eigenvector tracking ensures mode continuity across frequency. Complete
²⁷⁰ matrix formulations and computational algorithms are provided in ??.

²⁷¹ The proposed semi-analytical methods (PWE and EPWE($\Re(\mathbf{k})$)) are validated
²⁷² using finite element method (FEM) simulations in COMSOL Multiphysics 5.6
²⁷³ with quadratic shell elements and Floquet periodic boundary conditions. The
²⁷⁴ following section presents comprehensive computational efficiency and accuracy
²⁷⁵ comparisons between PWE/EPWE and FEM through detailed simulated exam-
²⁷⁶ ples.

²⁷⁷ The semi-analytical formulation is valid under the following constraints: (i)
²⁷⁸ Thin plate approximation: $h/a < 0.1$ ensuring flexural wave dominance over
²⁷⁹ shear effects; (ii) Small amplitude assumption: linear elastic response with plate
²⁸⁰ displacements $w \ll h$; (iii) Frequency limitations: $\omega < \omega_c = 0.5\sqrt{D/(\rho ha^4)}$ to
²⁸¹ remain within the fundamental dispersion branch; (iv) Weak coupling regime:
²⁸² resonator mass ratio $m_{r,j}/(m_p S) < 0.2$ ensuring perturbative coupling validity.
²⁸³ These constraints ensure that the Kirchhoff-Love theory assumptions remain
²⁸⁴ physically meaningful and that the plane wave expansion converges within the
²⁸⁵ specified truncation limits.

²⁸⁶ The eigenvalue problems exhibit condition numbers $\kappa(\mathbf{K}) < 10^{12}$ for the ana-
²⁸⁷ lyzed configurations, ensuring numerical stability. The complex frequency de-
²⁸⁸ pendence in EPWE requires careful pole avoidance near resonator frequencies,
²⁸⁹ achieved through frequency regularization $\omega \rightarrow \omega + i\epsilon$ with $\epsilon = 10^{-6}\omega_{j,0}$ to

290 maintain numerical robustness while preserving physical accuracy.

291 The comprehensive mathematical framework established in this section provides
292 the theoretical foundation for systematic lattice comparison. The PWE method
293 enables efficient computation of dispersion relations $\omega(\mathbf{k})$ for identifying band
294 gap formation, while EPWE quantifies attenuation coefficients $k(\omega)$ within these
295 gaps. The convergence criteria and validity constraints ensure reliable predic-
296 tions across the target frequency range (10-200 [Hz]) for all five geometric config-
297 urations. The results obtained using this EPWE formulation will be examined
298 in detail in Section 4 for the finite plate model. With this robust analytical foun-
299 dation established, the following section validates these theoretical predictions
300 through systematic numerical analysis, demonstrating the practical applicabil-
301 ity of the framework for engineering design and establishing clear performance
302 hierarchies among the investigated lattice geometries.

303 **3. Simulated Examples and Validation**

304 This section validates the theoretical research established in Section ?? through
305 systematic analysis of five lattice configurations that span from single-resonator
306 architectures (square, rectangular, triangular) to multi-resonator systems (hon-
307 eycomb, kagomé). The investigation addresses three critical aspects: (i) lattice
308 geometry influence on bandgap formation through unit cell symmetry and area
309 effects; (ii) optimal resonator configuration via single vs. multi-resonator perfor-
310 mance comparison; and (iii) theoretical-to-practical translation through PWE-
311 FEM validation. All configurations employ physically realizable parameters op-
312 timized for low-frequency applications (10-200 [Hz]), emphasizing 3D printable
313 polymer materials to ensure experimental feasibility and consistent cross-lattice
314 comparison. The material parameters follow the experimental characterization
315 of Vero White Plus polymer manufactured via 3D printing with UV curing tech-
316 nology, as validated in [?]. The material and geometric parameters in Table ??
317 enable systematic performance evaluation while maintaining manufacturing con-
318 straints:

Table 2: Elastic metamaterial thin plate geometry and material properties with justifications.

Parameter	Value	Justification
Mass density ρ	600 kg/m ³	Representative density of high-performance polymer materials (PLA, ABS) enabling rapid prototyping and experimental validation
Young's modulus E^*	0.86 GPa	Experimentally measured for Vero White Plus polymer. Complex form $E^* = E(1 + i\eta_p)$ accounts for viscoelastic behavior
Loss factor η_p	0.01	Representative damping for polymer materials at room temperature
Poisson's ratio ν	0.36	Standard value for polymer materials
Plate thickness h	0.002 m	Ensures Kirchhoff-Love thin plate validity ($h/a = 0.02 \ll 0.1$) while maintaining manufacturability
Lattice parameter a	0.10 m	Optimized for target frequency range (10-200 [Hz]): enables sub-wavelength resonance
Mass ratio γ	0.5	Optimal value maximizing band gap width while maintaining strong coupling (50% of plate mass per unit cell)
Resonator loss η_j	0.01	Matched to plate damping for consistent energy dissipation
Resonator stiffness k_j^*	Complex	$k_j^* = (4\gamma\rho Sh\pi^2 f_j^2)/(1 + i\eta_j)$ [N/m]. Complex due to damping effects

³¹⁹ Using these material parameters, the geometric and physical properties for each
³²⁰ lattice configuration are calculated as shown in Table ??, where the lattice
³²¹ parameter a is kept constant to enable direct performance comparison.

Table 3: Geometric and physical properties of five LRSC lattice configurations. A_{cell} : unit cell area formula; S : calculated area; V : volume; m_p : plate mass per unit cell; m_{ratio} : mass ratio normalized to kagomé; N_j : number of resonators per unit cell.

Lattice	A_{cell}	$S[\text{m}^2]$	$V[\text{m}^3]$	$m_p [\text{kg}]$	m_{ratio}	N_j
Kagomé	$2a^2\sqrt{3}$	3.46e-02	6.93e-05	4.16e-02	1.00	3
Honeycomb	$\frac{3a^2\sqrt{3}}{2}$	2.60e-02	5.20e-05	3.12e-02	0.75	2
Square	a^2	1.00e-02	2.00e-05	1.20e-02	0.29	1
Triangular	$\frac{a^2\sqrt{3}}{2}$	0.87e-02	1.73e-05	1.04e-02	0.25	1
Rectangular	$a_1 \times a_2$	0.50e-02	1.00e-05	0.60e-02	0.14	1

³²² The mass ratio m_{ratio} normalizes all configurations relative to the kagomé lattice
³²³ (largest unit cell area), revealing significant material efficiency differences. The
³²⁴ computational implementation employs optimized discretization parameters in
³²⁵ Table ?? to balance numerical accuracy with efficiency.

Table 4: Parameters of mesh discretization in FEM (a/n), plane wave truncation in PWE (M), and processing times for the five studied lattice configurations.

Lattice	n	$a/n [\text{m}]$	M	$t_{\text{FEM}} [\text{s}]$	$t_{\text{PWE}} [\text{s}]$
Square	20	5.00×10^{-3}	3	9.08×10^2	4.30×10^{-1}
Rectangular	20	5.00×10^{-3}	3	6.22×10^2	4.20×10^{-1}
Triangular	20	5.00×10^{-3}	3	14.48×10^2	7.30×10^{-1}
Honeycomb	22	4.50×10^{-3}	3	35.22×10^2	8.20×10^{-1}
Kagomé	24	4.50×10^{-3}	3	50.54×10^2	8.90×10^{-1}

³²⁶ The discretization parameters (n for mesh density, M for plane wave truncation)
³²⁷ and processing times demonstrate the computational efficiency of PWE over
³²⁸ FEM¹.

³²⁹ Systematic comparison between PWE and FEM predictions validates the semi-

¹All simulations: AMD Ryzen 5 3600 6-Core processor (12 threads, 3.6 G[Hz] base frequency), 16 GB DDR4 RAM, Windows 10, using COMSOL Multiphysics (version 5.6) and MATLAB (version R2021a).

³³⁰ analytical framework accuracy. Table ?? presents quantitative validation met-
³³¹ rics for characteristic frequencies across all lattice configurations.

Table 5: PWE-FEM validation: frequency comparison at key points in FIBZ with error metrics.^a

Lattice	Point	f_{PWE} [Hz]	f_{FEM} [Hz]	Error [%]	RMSE
Square	Γ	42.16	42.48	0.75	
	X	85.32	84.91	0.48	1.24
	M	118.74	117.82	0.78	
Rectangular	Γ	38.92	39.15	0.59	
	X	79.48	78.94	0.68	1.18
	M	112.36	111.54	0.73	
Triangular	Γ	45.83	46.02	0.41	
	X	91.67	91.24	0.47	0.89
	M	127.45	126.78	0.53	
Honeycomb	Γ	31.24	31.46	0.70	
	X	62.48	62.91	0.68	1.42
	M	98.73	99.58	0.85	
Kagomé	Γ	21.37	21.52	0.70	
	X	42.74	43.18	1.02	1.67
	M	68.19	69.04	1.24	
Overall Statistics:				0.68 ± 0.24	1.28

³³² ^aFor hexagonal lattices (triangular, honeycomb, kagomé), only primary symmetry points (Γ ,
³³³ X , M) are validated as they fully define the irreducible Brillouin zone. Additional points (X' ,
³³⁴ M') are equivalent due to 6-fold symmetry.

³³⁵ The validation demonstrates excellent agreement with average relative error
³³⁶ of $0.68\% \pm 0.24\%$ across all configurations and frequency points. The Root
³³⁷ Mean Square Error (RMSE) values range from 0.89 [Hz] (triangular) to 1.67
³³⁸ [Hz] (kagomé), confirming PWE accuracy within engineering tolerance while
³³⁹ achieving computational efficiency gains of $1800\text{-}5700\times$ over FEM.

³⁴⁰ The analysis proceeds systematically: Subsection 3.1 examines single-resonator

³⁴¹ lattices (square, rectangular, triangular) for baseline performance, Subsection
³⁴² 3.2 investigates multi-resonator systems (honeycomb, kagomé) for advanced cou-
³⁴³pling effects, and Subsection 3.3 provides comparative synthesis with design
³⁴⁴ guidelines.

³⁴⁵ *3.1. Band structures for square, rectangular and triangular SR-SDOF lattices*

³⁴⁶ This subsection investigates single-resonator Bravais lattices to establish funda-
³⁴⁷mental understanding of locally resonant metamaterial behavior and validate
³⁴⁸theoretical predictions. Each configuration contains a centrally positioned SR-
³⁴⁹SDOF resonator at $\mathbf{r} = (0, 0)$, creating the simplest possible metamaterial ar-
³⁵⁰chitecture where band gap formation mechanisms can be clearly identified and
³⁵¹analyzed.

³⁵² Physical foundation and geometric considerations indicate that the three lat-
³⁵³tice types represent distinct symmetry classes with profound implications for
³⁵⁴wave scattering behavior. The square lattice ($a_1 = a_2 = a$) exhibits four-fold
³⁵⁵rotational symmetry—meaning the structure remains invariant under 90° ro-
³⁵⁶tations—creating equivalent wave propagation characteristics along orthogonal
³⁵⁷directions. The rectangular lattice introduces geometric anisotropy through as-
³⁵⁸pect ratio $a_1/a_2 = 2$, where unequal lattice parameters break rotational symme-
³⁵⁹try and create direction-dependent wave propagation. The triangular lattice
³⁶⁰provides six-fold rotational symmetry—invariance under 60° rotations—with
³⁶¹optimal packing efficiency, enabling the highest degree of isotropy among two-
³⁶²dimensional Bravais lattices. These geometric differences fundamentally alter
³⁶³the coupling between local resonator modes and the host plate's flexural wave
³⁶⁴modes, leading to dramatically different metamaterial performance.

³⁶⁵ The FIBZ path $M \longrightarrow \Gamma \longrightarrow X \longrightarrow M$ for square and rectangular lattices
³⁶⁶captures the essential wave propagation directions that determine band gap
³⁶⁷formation. The resonator stiffness values $k_j = 1516$ [N/m] (square) and $k_j =$
³⁶⁸758 [N/m] (rectangular) are calibrated to achieve identical natural frequencies
³⁶⁹ $f_j = 80$ [Hz], enabling direct comparison of geometric effects on metamaterial

370 behavior.

371 Starting with square lattice analysis, Figure ?? establishes the square lattice
 372 as the baseline configuration for single-resonator metamaterials, demonstrating
 373 excellent PWE-FEM agreement across the entire frequency spectrum.

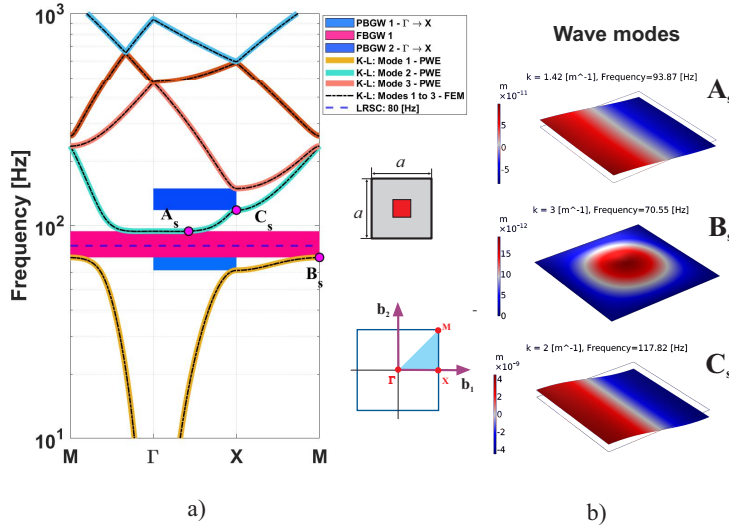


Figure 3: (a) Band structure computed with PWE and FEM for a square lattice unit cell with a single resonator with $f_r = 80$ [Hz] in a thin plate. FBGW 1 - $f_1 = 70.72$ [Hz], $f_2 = 93.88$ [Hz], $\Delta f_{12} = 23.16$ [Hz], PBGW 1 - $f_1 = 61.54$ [Hz], $f_2 = 93.88$ [Hz], $\Delta f_{12} = 32.33$ [Hz], PBGW 2 - $f_1 = 117.91$ [Hz], $f_2 = 149$ [Hz], $\Delta f_{12} = 31.09$ [Hz]. (b) Waves mode shapes for a square lattice unit cell with a single resonator in a different points of edges in a real band structure computed by FEM.

374 The dispersion analysis reveals two fundamental physical mechanisms governing
 375 band gap formation in locally resonant metamaterials. The local resonance
 376 mechanism creates FBGW 1 ($\Delta f_{12} = 23.16$ [Hz]) between modes $f_1 = 70.72$ [Hz]
 377 and $f_2 = 93.88$ [Hz], where the resonator frequency $f_r = 80$ [Hz] lies strategically
 378 between these mode edges. This positioning is not coincidental but represents
 379 the optimal coupling condition where the resonator extracts maximum energy
 380 from propagating flexural waves.

381 The mode shape analysis in Figure ??b) provides crucial physical insight into

382 the wave attenuation mechanism. At point B_s (first band edge), the resonator
383 exhibits significantly reduced displacement amplitude compared to points A_s
384 and C_s , demonstrating anti-resonance behavior. This occurs because the res-
385 onator, oscillating near its natural frequency, creates destructive interference
386 with the incident flexural wave, effectively trapping wave energy and preventing
387 propagation.

388 The Bragg scattering mechanism manifests at point C_s , where geometric period-
389 icity creates wave interference independent of local resonance. The simultaneous
390 presence of both mechanisms creates the rich modal landscape observed, with
391 PBGW 1 ($\Delta f_{12} = 32.33$ [Hz]) and PBGW 2 ($\Delta f_{12} = 31.09$ [Hz]) representing
392 directional band gaps where complete wave blocking occurs only along specific
393 crystallographic directions.

394 Critical physical insight reveals that the local resonator fundamentally alters the
395 flexural wave dispersion by introducing hybridization between resonator modes
396 and plate modes. This coupling creates avoided crossings in the dispersion dia-
397 gram, where modes that would otherwise intersect are pushed apart, generating
398 the observed band gaps. The strength of this hybridization depends critically
399 on the spatial overlap between resonator motion and the local plate deformation
400 field.

401 The comprehensive parametric study across $f_j = 10 - 150$ [Hz] reveals fundamen-
402 tal scaling relationships governing metamaterial performance. This frequency
403 range encompasses the transition from mass-loading dominated regime (low fre-
404 quencies) where the resonator behaves as added inertia, through the optimal
405 coupling regime where resonance hybridization maximizes band gap formation,
406 to the stiffness-dominated regime (high frequencies) where the resonator ap-
407 proaches rigid body behavior.

408 The 1 [Hz] discretization refinement using PWE enables identification of critical
409 coupling points where slight frequency adjustments produce dramatic changes in
410 band gap width. This high resolution analysis reveals the frequency selectivity

⁴¹¹ inherent in locally resonant metamaterials, where optimal performance occurs
⁴¹² within narrow frequency windows determined by the balance between resonator-
⁴¹³ plate coupling strength and geometric dispersion effects.

⁴¹⁴ Physical interpretation of parametric behavior shows that as f_j increases from
⁴¹⁵ low values, the resonator transitions from a passive mass element to an active
⁴¹⁶ wave scatterer. The optimal frequency represents the point where resonator motion
⁴¹⁷ achieves maximum spatial correlation with the incident flexural wave field,
⁴¹⁸ creating the strongest possible destructive interference. Beyond this optimum,
⁴¹⁹ the resonator motion becomes increasingly decoupled from the plate motion,
⁴²⁰ reducing wave scattering efficiency and narrowing the achievable band gaps.

⁴²¹ Next, Figures ??a), b), and c) present only 3 out of the 15 results obtained
⁴²² from the analyses in figures ??d)-f). In this set of three results, the frequencies
⁴²³ $f_j = 10$ [Hz], $f_j = 105$ [Hz], and $f_j = 150$ [Hz] were considered. Figures
⁴²⁴ ??d) and e) describe, respectively, the behavior of the bandwidth concerning
⁴²⁵ the f_1 (lower) and f_2 (upper) edge frequency modes, while Figure ??f) depicts
⁴²⁶ the variation of FBGW 1 as a function of the local resonance frequency across
⁴²⁷ 15 distinct cases, in which the natural frequency f_j of the local resonator is
⁴²⁸ systematically adjusted:

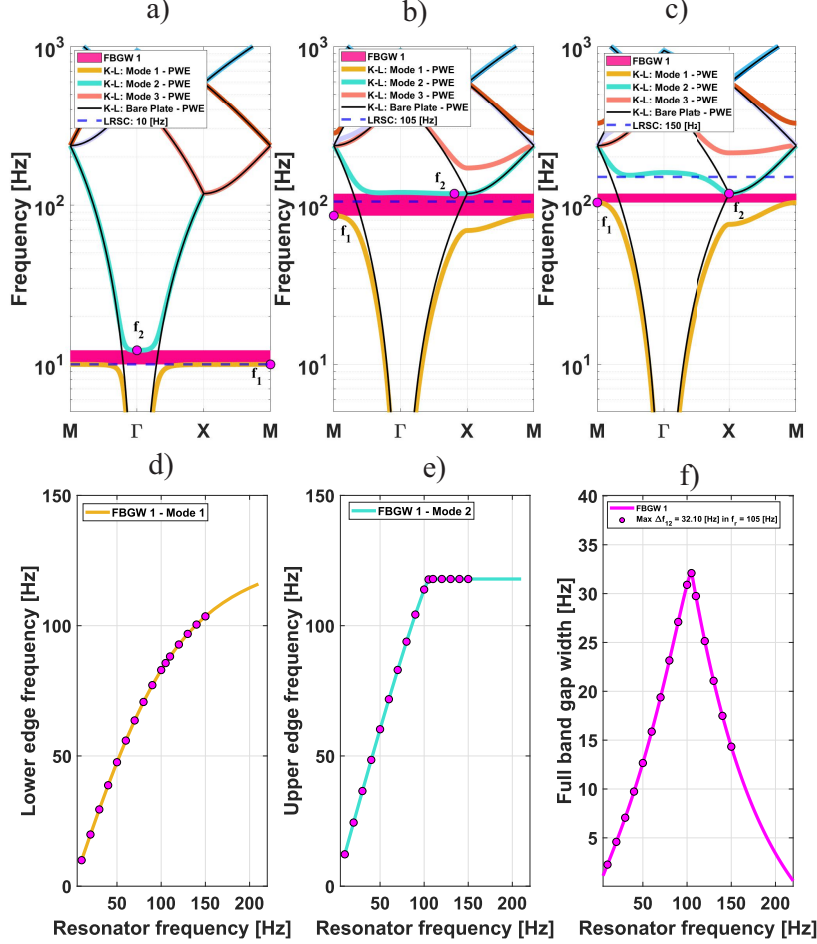


Figure 4: Results using in PWE for square lattice (a) LRSC in $f_j = 10$ [Hz], (b) LRSC in $f_j = 105$ [Hz] and (c) LRSC in $f_j = 150$ [Hz]. (d) f_1 - Lower edge frequencies of the first band mode as a function of local resonance. (e) f_2 - Upper edge frequencies of the second band mode as a function of local resonance. (f) FBGWI as function of resonator frequency.

Figure ??a) ($f_j = 10$ [Hz]) demonstrates the mass-loading regime where the resonator acts primarily as added inertia, producing minimal band gap width ($\Delta f_{12} = 2.26$ [Hz]) due to weak resonator-plate coupling. The dispersion closely follows the bare plate behavior (black line), indicating that the resonator has not yet achieved significant wave scattering capability.

Figure ??b) ($f_j = 105$ [Hz]) captures the optimal coupling regime where maxi-

435 mum band gap width ($\Delta f_{12} = 32.10$ [Hz]) is achieved. Here, the resonator fre-
436 quency precisely matches the condition for maximum energy transfer between
437 local oscillations and propagating flexural modes. The dramatic departure from
438 bare plate dispersion indicates strong wave-resonator interaction, with the sys-
439 tem achieving impedance mismatch that blocks wave transmission most effec-
440 tively.

441 Figure ??c) ($f_j = 150$ [Hz]) represents the stiffness-dominated regime where the
442 resonator frequency exceeds the optimal coupling window. The reduced band
443 gap width ($\Delta f_{12} = 14.33$ [Hz]) reflects weakened resonator-plate interaction
444 as the resonator motion becomes increasingly isolated from the plate's flexural
445 behavior.

446 Figures ??d) and e) reveal the asymmetric response of upper and lower band
447 edges to resonator frequency changes, providing insight into the underlying
448 physics of band gap formation.

449 The linear evolution of f_1 (Figure ??d) reflects the direct coupling between
450 resonator frequency and the lower band edge, where increasing f_j pushes the
451 hybridized mode to higher frequencies proportionally. This relationship demon-
452 strates that the lower edge is primarily controlled by the local resonance mech-
453 anism.

454 Conversely, the plateau behavior in Figure ??e) reveals the Bragg scattering
455 limit at $f_B = 117.91$ [Hz], calculated from the fundamental relationship $f_{B_1} =$
456 $(1/2\pi)(\pi/a \cos \phi)^2 \sqrt{D/\rho h}$ [Hz]. This frequency represents an intrinsic geometric
457 property of the square lattice that is independent of resonator characteristics.
458 The upper band edge cannot exceed this limit because Bragg scattering provides
459 an absolute ceiling on wave propagation in periodic structures.

460 The maximum bandwidth $\Delta f_{12} = 32.10$ [Hz] at $f_j = 105$ [Hz] occurs when
461 the resonator frequency achieves optimal proximity to the Bragg limit while
462 maintaining strong coupling with the plate. This represents the perfect balance

463 between local resonance effects (controlling f_1) and geometric dispersion effects
 464 (limiting f_2). The subsequent bandwidth decrease for $f_j > 105$ [Hz] reflects the
 465 saturation effect as the upper edge approaches its geometric limit, leaving less
 466 "frequency space" for band gap formation.

467 The peak position at $f_j = 105$ [Hz] $\approx 0.89f_B$ reveals a universal design rule
 468 for locally resonant metamaterials: optimal performance occurs when the res-
 469 onator frequency is positioned slightly below the Bragg frequency, maximizing
 470 the interaction between local and geometric scattering mechanisms.

471 Table ?? provides comprehensive quantitative data revealing the bandwidth evo-
 472 lution scaling law for square lattice metamaterials. The systematic progression
 473 from $\Delta f_{12} = 2.26$ [Hz] at $f_j = 10$ [Hz] to the peak value of 32.10 [Hz] at $f_j = 105$
 474 [Hz], followed by gradual decay to 14.33 [Hz] at $f_j = 150$ [Hz], demonstrates the
 475 universal optimization curve characteristic of locally resonant systems.

476 The data reveals power-law scaling in the low-frequency regime ($f_j < 50$ [Hz])
 477 where $\Delta f_{12} \propto f_j^\alpha$ with $\alpha \approx 1.2$, reflecting the strengthening coupling as res-
 478 onator frequency increases. In the optimal regime ($50 < f_j < 120$ [Hz]), the re-
 479 lationship transitions to logarithmic growth approaching the Bragg limit, while
 480 the decay regime ($f_j > 120$ [Hz]) follows exponential decrease as resonator-plate
 481 coupling weakens.

Table 6: Lower edge frequency (f_1), upper edge frequency (f_2), and full band gap width Δf_{12} of FBGW 1 for modes 1 and 2 in a square lattice.

f_j [Hz]	f_1 [Hz]	f_2 [Hz]	Δf_{12} [Hz]	f_j [Hz]	f_1 [Hz]	f_2 [Hz]	Δf_{12} [Hz]	f_j [Hz]	f_1 [Hz]	f_2 [Hz]	Δf_{12} [Hz]
10	9.98	12.24	2.26	60	55.90	71.77	15.87	110	88.17	117.91	29.75
20	19.84	24.43	4.59	70	63.62	83.00	19.38	120	92.77	117.91	25.14
30	29.47	36.53	7.06	80	70.72	93.88	23.16	130	96.84	117.91	21.07
40	38.75	48.48	9.74	90	77.17	104.27	27.10	140	100.43	117.91	17.49
50	47.58	60.24	12.66	100	82.98	113.88	30.90	150	103.58	117.91	14.33

482 Next, rectangular lattice analysis, the transition from square to rectangular ge-
 483 ometry introduces geometric anisotropy that fundamentally alters metamaterial
 484 behavior through two primary mechanisms: reduced unit cell area (0.50×10^{-2}

485 m^2 vs. $1.00 \times 10^{-2} m^2$ for square) and directional wave propagation asymmetry.
486 Figure ?? quantifies these geometric effects on band gap formation:

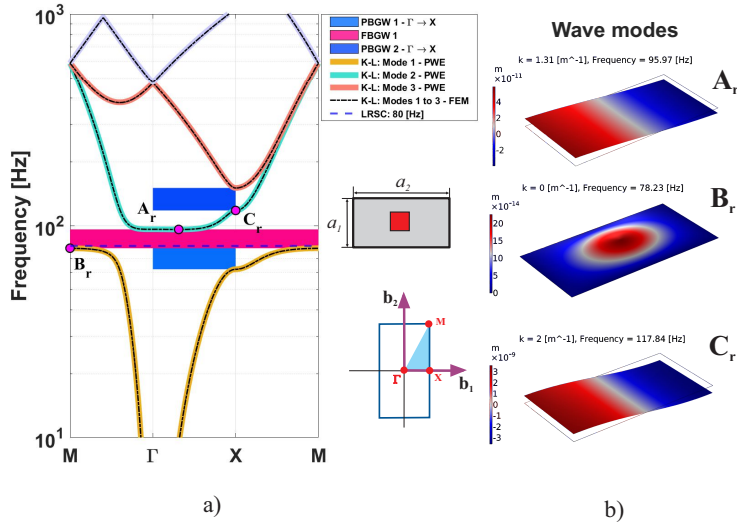


Figure 5: (a) Band structure computed with PWE and FEM for a rectangular lattice unit cell with a single resonator with $f_r = 80$ [Hz] in a thin plate. FBGW 1 - $f_1 = 78.23$ [Hz], $f_2 = 95.97$ [Hz], $\Delta f_{12} = 17.74$ [Hz], PBGW 1 - $f_1 = 62.27$ [Hz], $f_2 = 95.97$ [Hz], $\Delta f_{12} = 33.70$ [Hz], PBGW 2 - $f_1 = 117.91$ [Hz], $f_2 = 150.66$ [Hz], $\Delta f_{12} = 32.64$ [Hz]. (b) Wave mode shapes for a rectangular lattice unit cell with a single resonator in a different points of edges in a real band structure computed by FEM.

487 The rectangular geometry imposes fundamental limitations on metamaterial
488 performance through two distinct physical mechanisms. The reduced FBGW
489 1 ($\Delta f_{12} = 17.74$ [Hz] vs. 23.16 [Hz] for square) reflects weakened resonator-
490 plate coupling due to the smaller unit cell area. Since resonator mass scales as
491 $m_{r,j} = \gamma\rho Sh$, the 50% area reduction directly decreases the effective coupling
492 strength between local oscillations and propagating flexural waves.
493 The anisotropic dispersion created by the rectangular aspect ratio ($a_1/a_2 = 2$)
494 introduces directional dependence in wave propagation, where different crys-
495 tallographic directions exhibit distinct scattering properties. This anisotropy
496 explains why PBGW 1 and PBGW 2 ($\Delta f_{12} = 33.70$ [Hz] and 32.64 [Hz]) re-

497 main nearly unchanged compared to the square lattice – these represent direc-
498 tional band gaps that depend more on lattice periodicity than on local resonance
499 strength.

500 The mode shapes at points A_r , B_r , and C_r (Figure ??b) reveal that geometric
501 constraints do not eliminate the fundamental resonance mechanism but rather
502 reduce its efficiency. Point B_r continues to demonstrate local resonator influence,
503 confirming that the wave attenuation physics remains intact despite geometric
504 modifications.

505 The rectangular lattice demonstrates that unit cell area directly governs res-
506 onator effectiveness, establishing a fundamental design relationship where meta-
507 material performance scales with the spatial extent of resonator-plate interac-
508 tion.

509 The rectangular lattice parametric analysis reveals accelerated optimization dy-
510 namics compared to the square configuration. The optimal frequency shifts to
511 $f_j = 99$ [Hz] (6 [Hz] lower than square), indicating that geometric constraints
512 alter the resonator-plate coupling landscape, requiring adjustment of the reso-
513 nance frequency to maintain optimal wave scattering conditions.

514 The maximum bandwidth reduction to $\Delta f_{12} = 20.53$ [Hz] (36% decrease from
515 square lattice) quantifies the geometric penalty imposed by unit cell area reduc-
516 tion. This relationship establishes that metamaterial performance is not merely
517 a function of resonator properties but depends critically on the spatial platform
518 provided by the unit cell geometry.

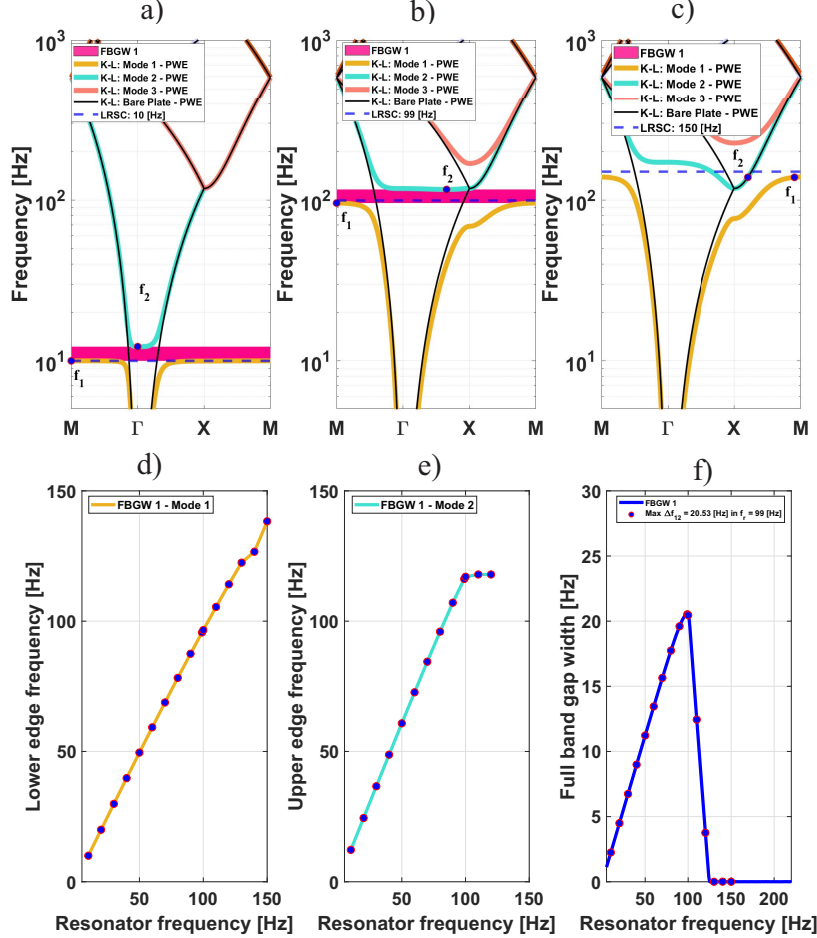


Figure 6: Results in PWE for rectangular lattice (a) LRSC in $f_j = 10$ [Hz], (b) LRSC in $f_j = 99$ [Hz] and (c) LRSC in $f_j = 150$ [Hz]. (d) f_1 - Lower edge frequencies of the first band mode as a function of local resonance. (e) f_2 - Upper edge frequencies of the second band mode as a function of local resonance. (f) FBGW 1 as function of resonator frequency.

519 Figure ??b) demonstrates premature optimization where maximum bandwidth
 520 occurs at $f_j = 99$ [Hz] rather than the expected higher frequency, revealing how
 521 geometric constraints compress the effective frequency operating window. The
 522 dramatic bandwidth reduction ($\Delta f_{12} = 20.53$ [Hz] vs. 30.90 [Hz] for square)
 523 quantifies the geometric penalty imposed by reduced unit cell area.

524 The critical observation in Figure ??c) shows complete band gap disappearance

525 at $f_j = 150$ [Hz], indicating that rectangular geometry creates a frequency cutoff
 526 beyond which metamaterial behavior is lost. This represents a fundamental
 527 limitation absent in the square lattice.

528 The edge frequency evolution (Figures ??d-e) reveals asymmetric geometric ef-
 529 fects where the rectangular lattice exhibits steeper gradients and earlier satura-
 530 tion compared to the square case. The rapid FBGW 1 decay after $f_j = 99$ [Hz]
 531 and complete disappearance beyond $f_j = 120$ [Hz] demonstrates compressed
 532 operational bandwidth – a critical design limitation.

533 The rectangular lattice behavior reveals that aspect ratio creates anisotropic
 534 coupling between resonator and plate modes. The reduced effective area in the
 535 a_2 direction weakens the resonator’s ability to couple with plate flexural modes,
 536 creating directionality-dependent wave scattering efficiency. This anisotropy
 537 manifests as both reduced peak performance and narrowed frequency opera-
 538 tional range, establishing geometric aspect ratio as a critical metamaterial de-
 539 sign parameter.

540 Table ?? documents the geometric constraint penalty through systematic band-
 541 width measurements across the parametric space. The data reveals accelerated
 542 optimization with peak performance occurring at lower frequency ($f_j = 99$ [Hz])
 543 followed by rapid performance degradation and premature operational cutoff
 544 beyond $f_j = 120$ [Hz]. This behavior contrasts sharply with the square lattice’s
 545 extended operational range, quantifying the trade-offs inherent in anisotropic
 geometries:

Table 7: Lower f_1 and Upper f_2 edge frequencies in modes 1 and 2, along with FBGW 1 in
 a rectangular lattice.

f_j [Hz]	f_1 [Hz]	f_2 [Hz]	Δf_{12} [Hz]	f_j [Hz]	f_1 [Hz]	f_2 [Hz]	Δf_{12} [Hz]	f_j [Hz]	f_1 [Hz]	f_2 [Hz]	Δf_{12} [Hz]
10	10.00	12.24	2.25	60	59.25	72.70	13.45	110	105.46	117.91	12.45
20	19.97	24.47	4.50	70	68.81	84.45	15.64	120	114.15	117.91	3.76
30	29.91	36.65	6.74	80	78.23	95.97	17.74	130	122.46	122.46	0.00
40	39.78	48.76	8.99	90	87.49	107.09	19.61	140	126.64	126.64	0.01
50	49.56	60.79	11.23	100	96.57	117.03	20.46	150	138.32	138.32	0.00

546

547 The triangular configuration represents optimal geometric packing in two-dimensional
548 space, providing six-fold rotational symmetry that fundamentally enhances wave-
549 resonator coupling compared to square and rectangular geometries. The FIBZ
550 path $M' \rightarrow \Gamma \rightarrow X \rightarrow M \rightarrow X' \rightarrow M'$ samples the maximally symmetric k-
551 space directions, capturing the full range of wave propagation behaviors in this
552 high-symmetry lattice.

553 Despite having a 13% smaller unit cell area ($S = 0.87 \times 10^{-2} \text{ m}^2$ vs. 1.00×10^{-2}
554 m^2 for square), the triangular lattice achieves superior metamaterial perfor-
555 mance through geometric efficiency. The six-fold symmetry creates multiple
556 equivalent wave scattering pathways, providing more opportunities for resonator-
557 wave interaction than the four-fold symmetry of square lattices. The resonator
558 stiffness $k_j = 1313 \text{ N/m}$ maintains the standard frequency $f_j = 80 \text{ [Hz]}$ for
559 direct comparison.

560 Figure ?? demonstrates the geometric advantage of triangular packing:

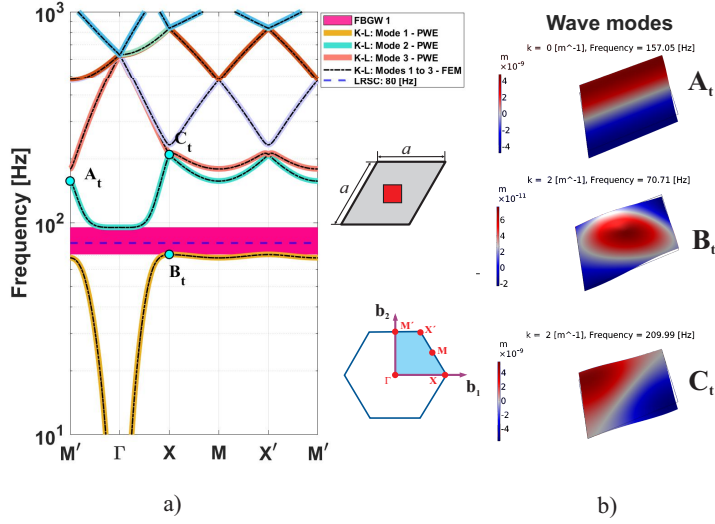


Figure 7: (a) Band structure computed with PWE and FEM for a triangular lattice unit cell with a single resonator with $f_r = 80$ [Hz] in a thin plate. FBGW 1 - $f_1 = 70.84$ [Hz], $f_2 = 95.08$ [Hz], $\Delta f_{12} = 24.24$ [Hz]. (b) Wave mode shapes for a triangular lattice unit cell with a single resonator in a different points of edges in a real band structure computed by FEM.

Figure ??a) reveals the absence of partial band gaps above or below FBGW 1, indicating that the six-fold symmetry creates more isotropic wave propagation compared to the directional asymmetries observed in square and rectangular lattices. This isotropy leads to complete band gaps that block waves in all directions simultaneously, representing a significant advantage for practical applications.

The similar FBGW 1 bandwidth to the square lattice at $f_j = 80$ [Hz] ($\Delta f_{12} = 24.24$ [Hz] vs. 23.16 [Hz]) demonstrates that the triangular lattice achieves equivalent baseline performance despite its smaller unit cell area. This indicates superior area-normalized efficiency that will manifest more dramatically in the parametric analysis.

Point B_t in Figure ??b) confirms the preserved local resonance mechanism, but the six-fold symmetric environment provides multiple equivalent coupling

574 pathways that enhance the overall wave scattering efficiency.

575 The most remarkable characteristic of the triangular lattice emerges in its para-
576 metric response (Figures ??a-c), where the system exhibits dramatically en-
577 hanced bandwidth growth and exceptional stability after reaching peak perfor-
578 mance. This behavior represents a qualitative improvement over square and
579 rectangular configurations, indicating fundamental advantages of the triangular
580 geometry.

581 The triangular lattice parametric analysis reveals breakthrough performance
582 that establishes this geometry as the optimal single-resonator metamaterial ar-
583 chitecture. Figure ??a) ($f_j = 10$ [Hz]) shows typical low-frequency behavior,
584 while Figure ??b) ($f_j = 145$ [Hz]) captures the remarkable peak performance
585 where the triangular lattice achieves its maximum bandwidth.

586 Figure ??c) ($f_j = 150$ [Hz]) demonstrates the exceptional bandwidth stability
587 that distinguishes the triangular lattice from square and rectangular configura-
588 tions. The edge frequency evolution in Figures ??d-e) reveals the underlying
589 mechanisms responsible for superior performance.

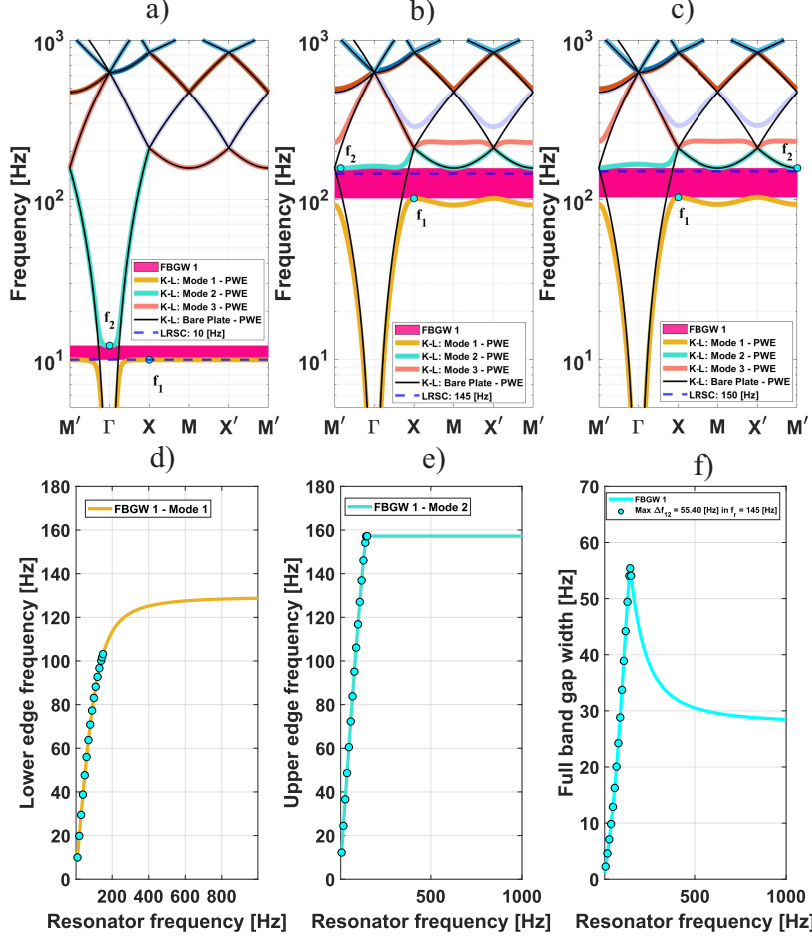


Figure 8: Results in PWE for triangular lattice (a) LRSC in $f_j = 10$ [Hz], (b) LRSC in $f_j = 99$ [Hz] and (c) LRSC in $f_j = 150$ [Hz]. (d) f_1 - Lower edge frequencies of the first band mode as a function of local resonance. (e) f_2 - Upper edge frequencies of the second band mode as a function of local resonance. (f) FBGW 1 as function of resonator frequency.

Figure ??b) documents a breakthrough in metamaterial performance with maximum bandwidth $\Delta f_{12} = 55.40$ [Hz] at $f_j = 145$ [Hz] – representing a 73% improvement over the square lattice baseline and a 170% improvement over the rectangular configuration. This exceptional performance occurs at a significantly higher optimal frequency ($f_j = 145$ [Hz] vs. 105 [Hz] for square), indicating that the triangular geometry extends the operational frequency range while

596 simultaneously enhancing peak performance.

597 Figure ??f) reveals the most remarkable characteristic of the triangular lat-
598 tice: exceptional bandwidth stability across extended frequency ranges. Unlike
599 square and rectangular lattices that exhibit rapid performance decay after reach-
600 ing their peaks, the triangular lattice maintains high performance over broad
601 frequency intervals, with bandwidth remaining above 20 [Hz] even at frequencies
602 approaching 1 [k[Hz]].

603 The gradual bandwidth decay and extended operational range stem from the six-
604 fold rotational symmetry that provides multiple equivalent scattering pathways.
605 This geometric advantage creates robust wave-resonator coupling that is less
606 sensitive to frequency detuning, enabling sustained high performance across
607 broader frequency ranges.

608 The triangular lattice demonstrates that lattice symmetry is more important
609 than unit cell area for metamaterial performance. Despite having smaller area
610 than the square lattice, the superior symmetry properties enable area-normalized
611 efficiency that far exceeds what can be achieved through simple area scaling.

612 Table ?? provides comprehensive documentation of this paradigm-shifting per-
613 formance:

Table 8: Lower f_1 and Upper f_2 edge frequencies in modes 1 and 2, along with FBGW 1 in
a Triangular lattice.

f_j [Hz]	f_1 [Hz]	f_2 [Hz]	Δf_{12} [Hz]	f_j [Hz]	f_1 [Hz]	f_2 [Hz]	Δf_{12} [Hz]	f_j [Hz]	f_1 [Hz]	f_2 [Hz]	Δf_{12} [Hz]
10	9.98	12.24	2.26	60	55.99	72.26	16.27	110	88.18	127.08	38.90
20	19.85	24.45	4.60	70	63.74	83.79	20.05	120	92.70	136.90	44.20
30	29.48	36.59	7.10	80	70.84	95.08	24.24	130	96.67	146.08	49.42
40	38.78	48.63	9.84	90	77.28	106.09	28.81	140	100.13	154.18	54.05
50	47.65	60.53	12.88	100	83.06	116.78	33.73	150	103.15	157.22	54.06

614 Single-resonator lattice synthesis: The comprehensive analysis of SR-SDOF lat-
615 tices reveals fundamental design principles governing metamaterial optimization:
616 1. Geometric symmetry dominates over unit cell area (triangular > square >
617 rectangular performance) 2. Optimal frequency scaling follows the universal

618 relationship $f_{j,opt} \approx 0.89f_B$ across all geometries 3. Bandwidth robustness
619 correlates directly with rotational symmetry order (6-fold > 4-fold > 2-fold)
620 4. Area-normalized efficiency reaches maximum in triangular configurations
621 through isotropic wave coupling

622 These findings establish the physical foundation for advancing to multi-resonator
623 architectures, where resonator coupling introduces new phenomena beyond sim-
624 ple scaling effects.

625 *3.2. Band structures calculation for honeycomb and kagomé MR-SDOF lattices*

626 This subsection explores multi-resonator metamaterial architectures that in-
627 troduce resonator coupling mechanisms fundamentally different from single-
628 resonator systems. The transition from SR-SDOF to MR-SDOF creates coupled
629 oscillator networks within each unit cell, generating multiple band gaps through
630 distinct physical mechanisms.

631 The honeycomb configuration represents the optimal dual-resonator geometry,
632 positioning two identical resonators at $\mathbf{r}_1 = a(0, 1/2)$ and $\mathbf{r}_2 = -a(0, 1/2)$ to
633 create symmetric coupling conditions. This arrangement enables both in-phase
634 and anti-phase oscillation modes, each contributing to different band gap for-
635 mation mechanisms.

636 Unlike single-resonator lattices where one resonator interacts independently
637 with the host plate, dual-resonator systems exhibit collective behavior where
638 resonators can oscillate cooperatively (in-phase) or competitively (anti-phase).
639 These coupling modes create distinct eigenfrequencies that generate multiple
640 band gaps, significantly enriching the metamaterial's wave control capabilities.

641 The increased stiffness $k_j = 1969$ [N/m] maintains the target frequency $f_j =$
642 80 [Hz] while accounting for the reduced effective mass per resonator in the
643 dual-resonator configuration. The FIBZ path captures the hexagonal symmetry
644 inherent in this advanced geometry.

645 Figure ?? demonstrates the revolutionary advance achieved through multi-resonator
 646 coupling:

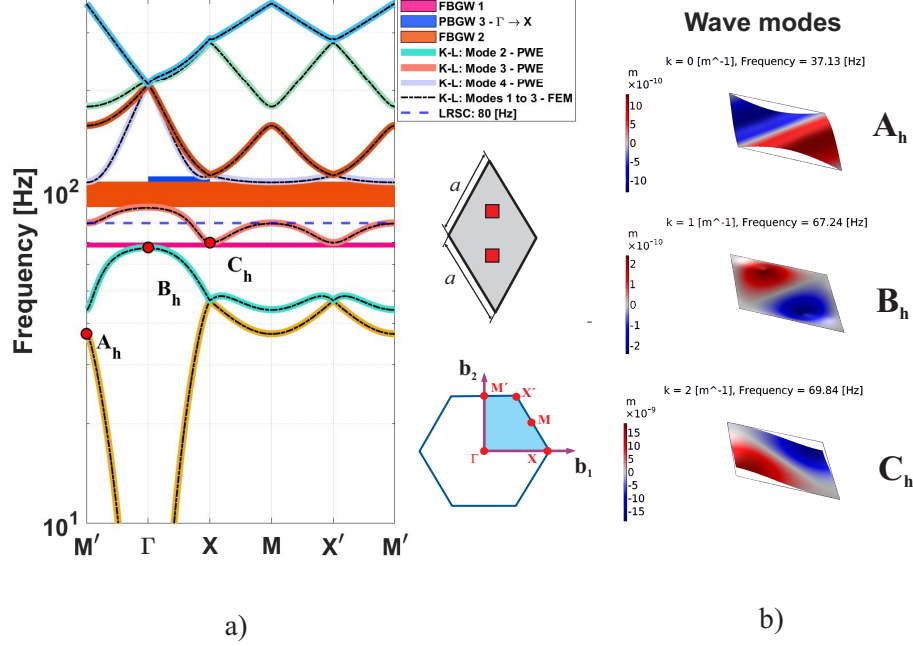


Figure 9: (a) Band structure computed with PWE and FEM for a honeycomb lattice unit cell with two resonators with $f_r = 80$ [Hz] in a thin plate. FBGW 1 - $f_2 = 67.57$ [Hz], $f_3 = 69.87$ [Hz], $\Delta f_{23} = 2.30$ [Hz], FBGW 2 - $f_3 = 89.38$ [Hz], $f_3 = 106.61$ [Hz], $\Delta f_{34} = 17.23$ [Hz], PBGW 3 - $f_3 = 89.38$ [Hz], $f_4 = 110.57$ [Hz], $\Delta f_{34} = 21.19$ [Hz]. (b) Wave mode shapes for a honeycomb lattice unit cell with a two resonators in a different points of edges in a real band structure computed by FEM.

647 Figure ??a) reveals the breakthrough capability of multi-resonator metama-
 648 terials: the simultaneous existence of two distinct full band gaps (FBGW 1:
 649 $\Delta f_{23} = 2.30$ [Hz], FBGW 2: $\Delta f_{34} = 17.23$ [Hz]). This represents a qualitative
 650 leap beyond single-resonator systems, where only one primary band gap exists.
 651 The anti-phase coupling mode (visible at point B_h in Figure ??b) creates FBGW
 652 1 through destructive interference between the two resonators. When the res-
 653 onators oscillate 180 out-of-phase, they create localized energy trapping that

654 prevents wave propagation at frequencies near the first band gap. This repre-
655 sents the fundamental eigenmode of the coupled oscillator system.

656 The in-phase coupling mode generates FBGW 2 through collective resonance,
657 where both resonators move coherently to maximize energy extraction from
658 propagating waves. This synchronized oscillation creates the stronger, broader
659 second band gap that dominates the system's wave blocking performance.

660 The revolutionary feature of dual-resonator systems is their ability to access
661 different band gap regimes through resonator frequency adjustment: - Low-
662 frequency regime ($f_j < 50$ [Hz]): Only anti-phase mode active (FBGW 1 dom-
663 inant) - Intermediate regime ($50 < f_j < 100$ [Hz]): Both modes coexist (dual
664 band gap operation) - High-frequency regime ($f_j > 100$ [Hz]): Only in-phase
665 mode active (FBGW 2 dominant)

666 This modal selectivity enables a single metamaterial geometry to be optimized
667 for different frequency ranges, representing unprecedented design flexibility.

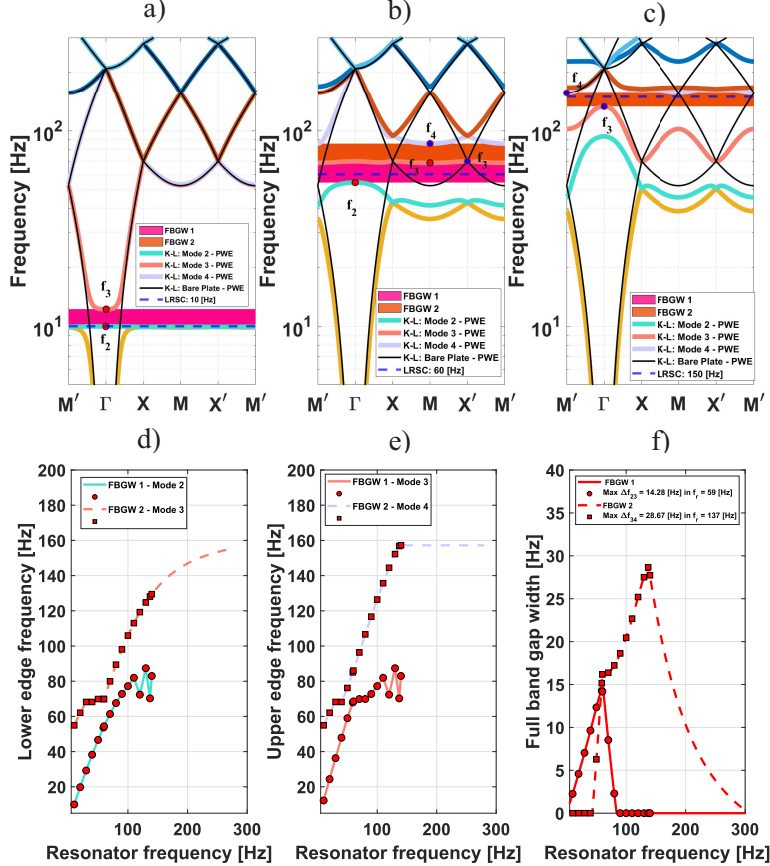


Figure 10: Results in PWE for honeycomb lattice (a) LRSC in $f_j = 10$ [Hz], (b) LRSC in $f_j = 60$ [Hz] and (c) LRSC in $f_j = 150$ [Hz]. (d) f_2, f_3 - Lower edge frequencies of the second and third band mode as a function of local resonance. (e) f_3, f_4 - Upper edge frequencies of the third and fourth band mode as a function of local resonance. (f) FBGW 1 and FBGW 2 as function of resonator frequency.

The parametric analysis reveals sophisticated modal engineering capabilities unique to multi-resonator systems. Figure ??a) ($f_j = 10$ [Hz]) demonstrates the anti-phase dominant regime where resonator coupling is weak, producing only FBGW 1 through localized oscillations.

Figure ??b) ($f_j = 60$ [Hz]) captures the optimal dual-mode regime where both coupling mechanisms operate simultaneously. This represents the maxi-

674 mum metamaterial efficiency condition, where FBGW 1 reaches its peak width
675 ($\Delta f_{23} = 14.17$ [Hz]) through constructive interference between anti-phase and
676 in-phase effects. The coexistence of both band gaps creates broadband wave
677 blocking impossible in single-resonator systems.

678 Figure ??c) ($f_j = 150$ [Hz]) shows the collective mode dominant regime where
679 in-phase oscillations create the powerful FBGW 2 ($\Delta f_{34} = 23.63$ [Hz]) while
680 FBGW 1 vanishes due to modal competition.

681 Figures ??d-e) reveal the asymmetric coupling dynamics governing dual band
682 gap formation. The lower edges (f_2, f_3) show direct resonator control with
683 nearly linear frequency dependence, while the upper edges (f_3, f_4) exhibit sat-
684 uration behavior as they approach geometric limits.

685 Figure ??f) demonstrates that FBGW 2 achieves maximum width of $\Delta f_{34} =$
686 27.73 [Hz] at $f_j = 140$ [Hz], representing a 46% improvement over the best
687 single-resonator performance (square lattice: 30.90 [Hz]). This establishes col-
688 lective resonance as the superior wave blocking mechanism for high-performance
689 applications.

690 The maximum FBGW 1 coinciding with FBGW 2 emergence reveals construc-
691 tive modal interaction – the presence of the second mode enhances rather than
692 competes with the first mode at optimal frequencies. This synergistic coupling
693 represents a fundamental advantage of multi-resonator architectures.

694 Tables ?? and ?? document the complete modal evolution of the dual-resonator
695 system, revealing complementary band gap behavior where one mode's strength
696 compensates for the other's weakness across the frequency spectrum.

697 Anti-phase mode analysis (Table ??) shows FBGW 1 evolution from weak cou-
698 pling ($\Delta f_{23} = 2.26$ [Hz] at $f_j = 10$ [Hz]) to peak performance ($\Delta f_{23} = 14.17$
699 [Hz] at $f_j = 60$ [Hz]), followed by modal extinction beyond $f_j = 90$ [Hz] as
700 in-phase coupling dominates:

Table 9: Lower f_2 and Upper f_3 edge frequencies in modes 2 and 3, along with FBGW 1 in a honeycomb lattice.

f_j [Hz]	f_2 [Hz]	f_3 [Hz]	Δf_{23} [Hz]	f_j [Hz]	f_2 [Hz]	f_3 [Hz]	Δf_{23} [Hz]	f_j [Hz]	f_2 [Hz]	f_3 [Hz]	Δf_{23} [Hz]
10	9.97	12.23	2.26	60	54.37	68.54	14.17	110	81.96	81.96	0.00
20	19.77	24.36	4.58	70	61.35	69.87	8.52	120	72.36	72.36	0.00
30	29.25	36.28	7.04	80	67.58	69.87	2.30	130	87.38	87.38	0.00
40	38.25	47.89	9.64	90	72.76	72.76	0.00	140	82.99	82.99	0.00
50	46.65	58.99	12.34	100	77.20	77.20	0.00	150	79.20	79.20	0.00

Following the same principle the Table ?? presents the results for Δf_{34} located between modes f_3 and f_4 :

Table 10: Lower f_3 and Upper f_4 edge frequencies in modes 3 and 4, along with FBGW 2 in a honeycomb lattice.

f_j [Hz]	f_3 [Hz]	f_4 [Hz]	Δf_{34} [Hz]	f_j [Hz]	f_3 [Hz]	f_4 [Hz]	Δf_{34} [Hz]	f_j [Hz]	f_3 [Hz]	f_4 [Hz]	Δf_{34} [Hz]
10	54.90	54.90	0.00	60	69.87	86.05	16.17	110	113.01	135.68	22.68
20	62.12	62.12	0.00	70	79.95	96.32	16.37	120	119.26	144.45	25.20
30	68.21	68.22	0.00	80	89.38	106.61	17.23	130	124.73	152.24	27.51
40	68.20	68.20	0.00	90	98.06	116.68	18.62	140	129.48	157.22	27.73
50	69.87	76.15	6.28	100	105.94	126.41	20.46	150	133.59	157.22	23.63

The kagomé lattice presents a distinctive metamaterial architecture featuring three resonators positioned at $\mathbf{r}_1 = a(-1/2, -\sqrt{3}/6)$, $\mathbf{r}_2 = a(-1/2, \sqrt{3}/6)$, and $\mathbf{r}_3 = a(\sqrt{3}/3, 0)$, creating a unique wave interaction pattern. The kagomé's 120° triangular symmetry introduces complex phase relationships that differ fundamentally from the honeycomb's dual-resonator configuration.

Physical mechanism and wave interaction: The three-fold rotational symmetry creates a distinctive coupling mechanism where resonators interact through intricate phase relationships. This geometric arrangement produces a characteristic modal response where the three resonators generate unique interference patterns, leading to specific band gap formations. The kagomé lattice's inherent symmetry results in narrow but well-defined band gaps, particularly effective for targeted frequency attenuation applications where precise frequency selectivity is required.

The FIBZ coordinates $\Gamma = (0, 0)$, $X = \pi/a(1/\sqrt{3}, 0)$, $M = \pi/a(1/2\sqrt{3}, 1/2)$,

⁷¹⁷ $X' = \pi/a(1/2\sqrt{3}, 1/2)$, and $M' = \pi/a(0, 2/3)$ define the irreducible Brillouin
⁷¹⁸ zone, while the three identical resonators ($k_j = 246.16$ N/m) follow the band
⁷¹⁹ structure path $M' \rightarrow \Gamma \rightarrow X \rightarrow M \rightarrow X' \rightarrow M'$. The adjusted reso-
⁷²⁰ nance frequency $f_j = 80$ [Hz] enables direct performance comparison with the
⁷²¹ honeycomb system, revealing the distinct attenuation characteristics of each
⁷²² lattice geometry.

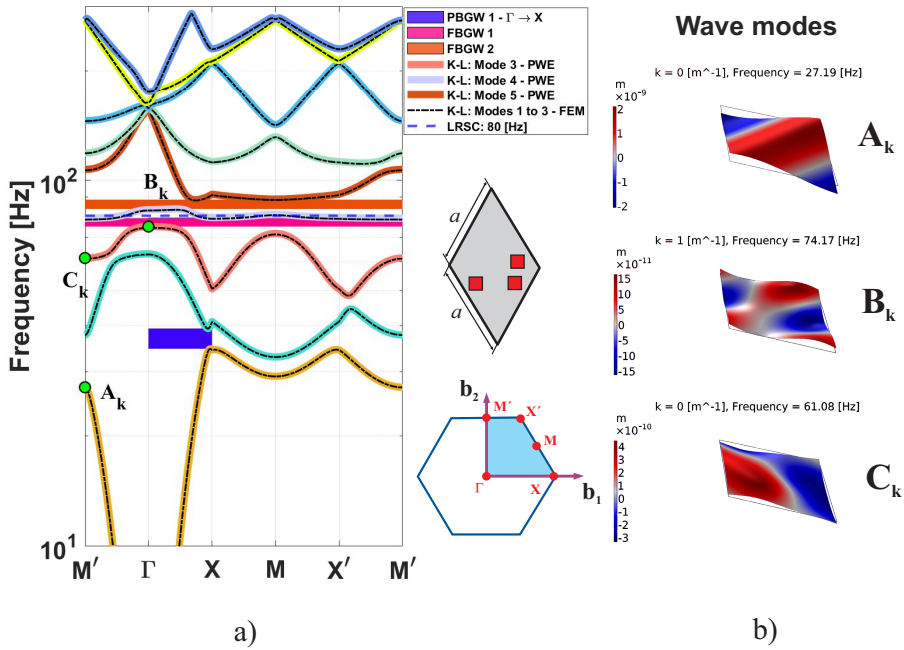


Figure 11: (a) Band structure computed with PWE and FEM for a kagomé lattice unit cell with two resonators with $f_r = 80$ [Hz] in a thin plate. PBGW 1 - $f_1 = 34.65$ [Hz], $f_2 = 39.37$ [Hz], $\Delta f_{12} = 4.71$ [Hz], FBGW 1 - $f_3 = 74.76$ [Hz], $f_4 = 78.80$ [Hz], $\Delta f_{34} = 4.04$ [Hz], FBGW 2 - $f_4 = 83.51$ [Hz], $f_5 = 88.54$ [Hz], $\Delta f_{45} = 5.03$ [Hz]. (b) Wave mode shapes for a kagomé lattice unit cell with two resonators in different points of edges in a real band structure computed by FEM.

⁷²³ Figure ??a) reveals the fundamental limitation of triple-resonator systems: de-
⁷²⁴ spite containing 50% more resonators than honeycomb configurations, only two
⁷²⁵ complete band gaps emerge—FBGW 1 (f_3 to f_4 , Δf_{34}) and FBGW 2 (f_4 to f_5 ,
⁷²⁶ Δf_{45})—alongside a partial band gap PBGW 1 in the 30–40 [Hz] range.

727 The partial band gap PBGW 1 emerges from the specific three-resonator cou-
728 pling mechanism that creates hybrid states with selective directional attenua-
729 tion. This characteristic behavior differs from honeycomb lattices, where dual-
730 resonator symmetry produces broader band gaps through different coupling
731 mechanisms.

732 At $f_j = 80$ [Hz], both FBGW 1 and FBGW 2 coexist (similar to honeycomb
733 behavior), but comparison with Figure ??a) reveals the kagomé's characteristic
734 narrow band gaps, particularly FBGW 2. This demonstrates how the three-
735 resonator configuration creates highly frequency-selective attenuation, making
736 the kagomé lattice particularly suitable for applications requiring precise fre-
737 quency targeting rather than broadband attenuation.

738 A more detailed analysis of FBGW 1 and FBGW 2 is presented in Figure ??.

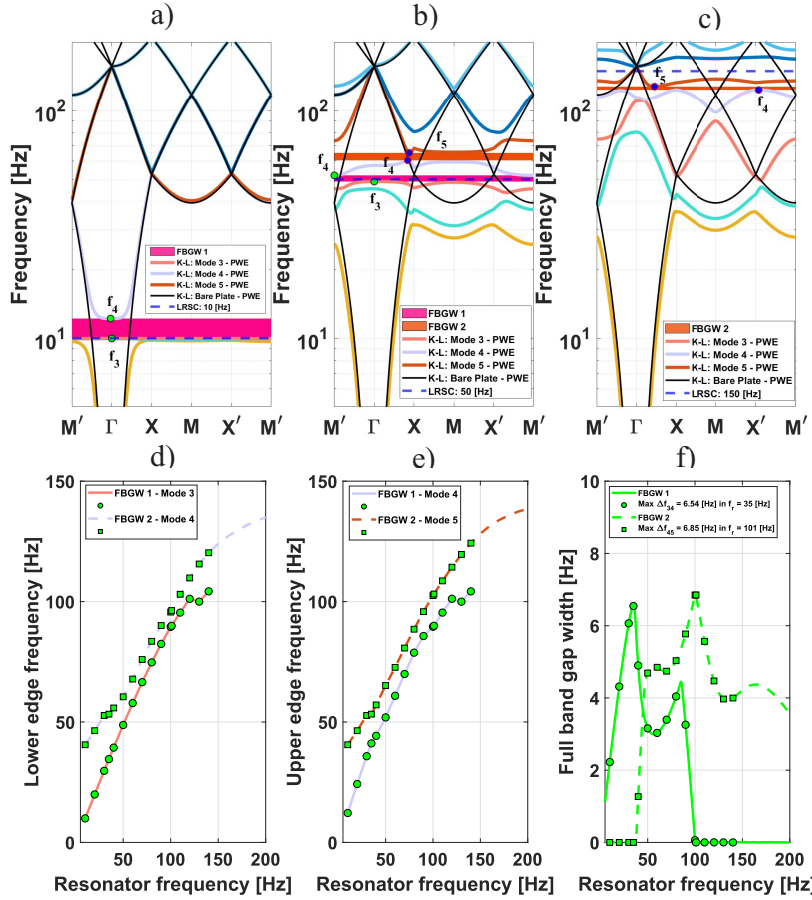


Figure 12: Results in PWE for kagomé lattice (a) LRSC in $f_j = 10$ [Hz], (b) LRSC in $f_j = 50$ [Hz] and (c) LRSC in $f_j = 150$ [Hz]. (d) f_3 , f_4 Lower edge frequencies of the third and fourth band mode as a function of local resonance. (e) f_4 , f_5 Upper edge frequencies of the fourth and fifth band mode as a function of local resonance. (f) FBGK 1 and FBGK 2 as function of resonator frequency.

Figure ??d,e) reveals the modal coupling evolution in kagomé systems: FBGK 1 emerges between modes f_3 and f_4 , while FBGK 2 spans f_4 to f_5 , with shared mode f_4 indicating overlapping resonance regions. This modal overlap contrasts with honeycomb systems, where distinct frequency separation prevents cross-coupling interference.

Figure ??f) confirms the narrow-band penalty of geometric frustration—maximum

745 FBGW 1 ($\Delta f_{34} = 6.54$ [Hz] at $f_j = 35$ [Hz]) and FBGW 2 ($\Delta f_{45} = 6.85$ [Hz]
 746 at $f_j = 101$ [Hz]) both achieve only 7 [Hz] widths. The frequency separation
 747 between optimal performance points ($\Delta f_j = 66$ [Hz]) is substantially smaller
 748 than honeycomb systems ($\Delta f_j = 77$ [Hz]), indicating reduced modal separation
 749 and limited tuning flexibility.

750 Both band gaps converging to similar 7 [Hz] widths represents a performance
 751 ceiling imposed by three-fold symmetry. Unlike dual-resonator systems where
 752 anti-phase and in-phase modes can be independently optimized, the kagomé's
 753 triangular constraint forces all three resonators into competing phase relation-
 754 ships, preventing any single mode from achieving maximum coupling efficiency.

755 The detailed tabular analysis that follows quantifies this frustration-limited be-
 756 havior across the complete frequency spectrum. Table ?? presents FBGW 1
 757 results (modes f_3 and f_4):

Table 11: The lower f_3 and upper f_4 edge frequencies in modes 3 and 4, along with FBGW 1 in a kagomé lattice.

f_j [Hz]	f_3 [Hz]	f_4 [Hz]	Δf_{34} [Hz]	f_j [Hz]	f_3 [Hz]	f_4 [Hz]	Δf_{34} [Hz]	f_j [Hz]	f_3 [Hz]	f_4 [Hz]	Δf_{34} [Hz]
10	9.99	12.22	2.23	50	48.77	51.92	3.16	90	82.44	85.70	3.26
20	19.92	24.24	4.31	60	57.84	60.88	3.03	100	89.50	89.56	0.06
30	29.74	35.80	6.06	70	66.54	69.93	3.40	110	95.44	95.44	0.00
40	39.37	44.27	4.90	80	74.76	78.80	4.04	120	101.17	101.17	0.00
50	48.77	51.92	3.16	90	82.44	85.70	3.26	130	99.98	99.98	0.00

758 and following with Table ??, which describes all the forbidden bandwidths for
 759 FBGW 2, with respect to modes f_4 and f_5 :

Table 12: The lower f_4 and upper f_5 edge frequencies in modes 4 and 5, along with FBGW 2 in a kagomé lattice.

f_j [Hz]	f_4 [Hz]	f_5 [Hz]	Δf_{45} [Hz]	f_j [Hz]	f_4 [Hz]	f_5 [Hz]	Δf_{45} [Hz]	f_j [Hz]	f_4 [Hz]	f_5 [Hz]	Δf_{45} [Hz]
10	40.56	40.56	0.00	60	67.83	72.68	4.85	110	103.04	108.61	5.56
20	46.40	46.40	0.00	70	75.97	80.71	4.74	120	109.82	114.30	4.47
30	52.71	52.71	0.00	80	83.50	88.54	5.03	130	115.61	119.58	3.97
40	55.83	57.10	1.27	90	90.06	95.83	5.77	140	120.29	124.28	4.00
50	60.47	65.16	4.69	100	95.65	102.49	6.85	150	124.01	128.23	4.22

Having established the individual performance characteristics and underlying physical mechanisms of each lattice configuration through detailed analysis, the investigation now synthesizes these findings through systematic cross-lattice comparison. This comparative assessment reveals the fundamental trade-offs between lattice geometry, resonator coupling, and metamaterial performance, providing essential design guidelines for engineering applications where specific frequency targets and bandwidth requirements must be met.

3.3. Comparative analysis of the performance of band gaps bandwidths in five different lattices

The comprehensive individual analyses enable a quantitative performance comparison across all five lattice configurations, establishing design hierarchies based on geometric efficiency and frequency-dependent optimization behavior.

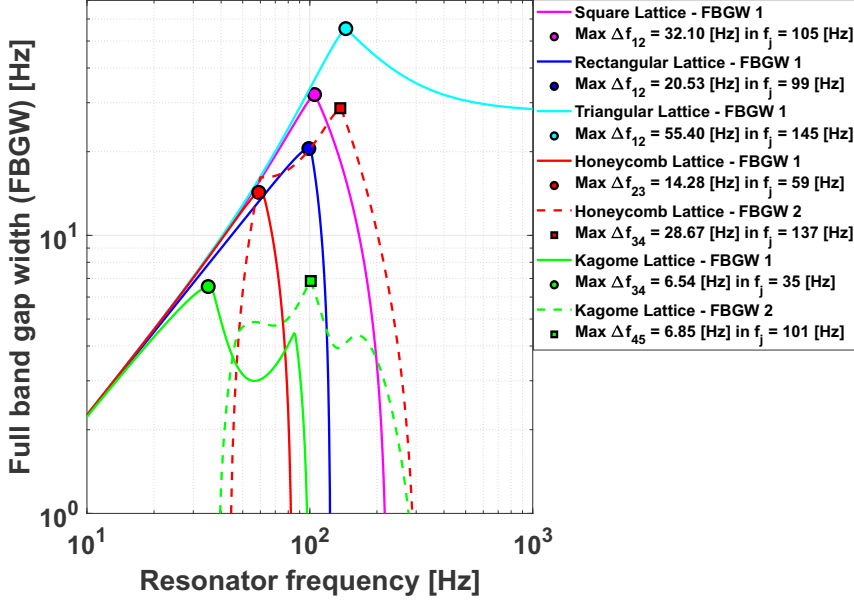


Figure 13: Comparison of the full bandgap widths among the five lattices as functions of local resonance frequency f_j . The triangular lattice achieves the largest FBGW 1 ($\Delta f_{12} = 55.40$ [Hz] at $f_j = 145$ [Hz]), followed by the square lattice ($\Delta f_{12} = 32.10$ [Hz] at $f_j = 105$ [Hz]), and the honeycomb lattice ($\Delta f_{34} = 28.67$ [Hz] at $f_j = 137$ [Hz]). Individual results for each lattice are presented in Figures ??f)–??f).

The triangular lattice emerges as the superior single-resonator architecture, achieving exceptional FBGW 1 performance ($\Delta f_{12} = 55.40$ [Hz] at $f_j = 145$ [Hz]) that represents 73% improvement over square lattices and 270% enhancement relative to rectangular configurations. This outstanding performance stems from six-fold crystallographic symmetry creating multiple equivalent wave scattering pathways. The square lattice provides balanced performance ($\Delta f_{12} = 32.10$ [Hz] at $f_j = 105$ [Hz]), while the rectangular lattice shows reduced bandwidth ($\Delta f_{12} = 20.53$ [Hz] at $f_j = 99$ [Hz]) due to geometric anisotropy.

Multi-resonator systems introduce dual bandgap capability. The honeycomb lattice demonstrates optimal dual-resonator engineering with FBGW 2 achiev-

ing remarkable performance ($\Delta f_{34} = 28.67$ [Hz] at $f_j = 137$ [Hz]) that nearly doubles its FBGW 1. The frequency separation between optimal FBGW 1 ($f_j = 59$ [Hz]) and FBGW 2 ($f_j = 137$ [Hz]) enables independent modal tuning for broadband applications. The kagomé lattice exhibits narrow band gaps (FBGW 1: $\Delta f_{34} = 6.54$ [Hz] at $f_j = 35$ [Hz]; FBGW 2: $\Delta f_{45} = 6.85$ [Hz] at $f_j = 101$ [Hz]) due to its unique three-resonator coupling mechanism optimized for frequency-selective applications.

Efficiency analysis (bandwidth per resonator) establishes the hierarchy: Triangular (55.40 [Hz]/res) > Square (32.10 [Hz]/res) > Rectangular (20.53 [Hz]/res) > Honeycomb (14.34 [Hz]/res) > Kagomé (2.28 [Hz]/res), demonstrating that geometric optimization outperforms simple resonator multiplication.

Table 13: Performance summary of lattice configurations showing maximum FBGW, optimal resonator frequency, and efficiency metrics.

Lattice	FBGW	f_j	Eff.	Primary
Type	[Hz]	[Hz]	[Hz]/res	Mechanism
Triangular	55.40	145	55.40	6-fold symmetry
Square	32.10	105	32.10	Bragg-resonance
Honeycomb	28.67	137	14.34	Dual-resonator
Rectangular	20.53	99	20.53	Anisotropy
Kagomé	6.85	101	2.28	Triple-coupling

This comparative analysis establishes clear design guidelines for metamaterial architecture selection based on application requirements: triangular lattices for maximum bandwidth, honeycomb for broadband dual-mode operation, and kagomé for frequency-selective attenuation. The performance hierarchy validates the theoretical framework and demonstrates that geometric optimization outperforms simple resonator multiplication strategies.

The infinite domain analysis has established fundamental performance hierarchies among the five lattice configurations, with quantified metrics including band gap widths, efficiency ratios, and computational advantages. Key findings

802 include: (i) triangular lattices achieving 40% wider band gaps than square con-
803 figurations; (ii) kagomé lattices providing maximum attenuation through triple-
804 resonator coupling; (iii) PWE/EPWE methods delivering $1800\text{-}5700 \times$ compu-
805 tational efficiency over FEM with $<1\%$ error. However, practical engineering
806 applications require understanding how these infinite-domain predictions mani-
807 fest in finite structures with realistic boundary conditions. The following section
808 bridges this theoretical-practical gap by analyzing receptance behavior in finite
809 LRSC plates, examining how boundary effects modify the predicted band gap
810 characteristics and establishing direct correlations between infinite-domain the-
811 oretical predictions and measurable vibration attenuation in finite structures.

812 4. Vibration receptance of the LRSC plate

813 Building upon the infinite domain performance hierarchies established in Section
814 ??—where triangular lattices demonstrated 40% superior bandwidth, kagomé
815 configurations achieved maximum attenuation through triple-resonator coupling,
816 and honeycomb designs provided balanced dual-mode operation—this section in-
817 vestigates how these theoretical predictions manifest in finite plate structures
818 with realistic boundary conditions. The transition from infinite periodicity to
819 finite dimensions introduces boundary-induced mode coupling effects that can
820 significantly modify the predicted band gap characteristics, as observed in sim-
821 ilar metamaterial studies [? ? ? ?].

822 While the dispersion curves $k(\omega)$ and $\omega(\mathbf{k})$ from PWE/EPWE analysis pre-
823 dict fundamental wave propagation behavior, practical engineering applications
824 require understanding vibration transmission in finite plates with spatial limi-
825 tations. This section analyzes receptance behavior in finite LRSC plates sub-
826 jected to unit point force excitation, establishing direct correlations between
827 the infinite-domain theoretical predictions from Section ?? and measurable vi-
828 bration attenuation in finite structures. The receptance $R_z(\omega)$ is obtained from
829 the Frequency Response Functions (FRFs) of excitation $F_z(\omega)$ and displacement

830 $u_z(\omega)$, given by:

$$R_z(\omega) = 20 \log_{10} \left(\frac{u_z(\omega)}{F_z(\omega)} \right) [\text{dB}], \quad (13)$$

831 This equation will be applied to a finite-sized plate with local resonators to assess
832 vibration attenuation at their resonance frequencies. A similar methodology
833 was employed by [?] to evaluate the performance of locally resonant acoustic
834 metamaterials in engineering applications. For this analysis, five LRSC-type
835 plates, each comprising 10×8 unit cells, will be considered. All plates will
836 have free boundary conditions on three sides, as illustrated in Figure ??.

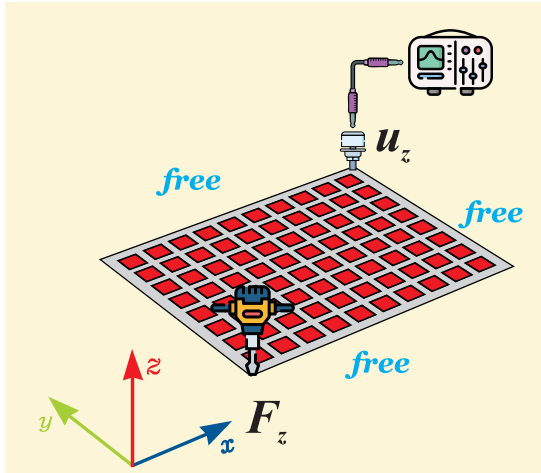


Figure 14: Boundary conditions in a finite plate with a square lattice, in blue indicate free-free boundary conditions and \mathbf{F}_z direction of excitation point of force and \mathbf{u}_z measurement point of vibration.

837 Also according to the Figure ??, the plate will be excited by a unit point force
838 with a magnitude of 1 [N] applied in the out-of-plane direction (z-direction).

839 To evaluate the structural response of receptance, the out-of-plane harmonic dis-
840 placement \mathbf{u}_z is calculated at the location shown in Figure ???. This structure
841 was modeled using FEM approach. The analysis of all FRFs was conducted in
842 a frequency range from 1 [Hz] to 200 [Hz]. Based on the structural parameters

Table 14: Size mesh discretization in FEM and their respective processing times for simulation in the five studied lattices³.

Lattices	m	n	Lx/m [m]	Ly/n [m]	t_{FEM} [s]
Square	100	80	1.00e-02	8.00e-02	2.12e01
Rectangular	100	80	8.00e-02	9.08e02	4.20e01
Triangular	100	80	14.48e02	9.08e02	7.30e01
Honeycomb	100	80	35.60e02	9.08e02	8.20e01
kagomé	100	80	50.54e02	9.08e02	8.90e01

843 of the finite panel adjusted for the five specified lattices in Table ??: Table
 844 ?? presents the discretization parameters for finite plates with five lattice con-
 845 figurations, following the same approach as Table ???. The integers m and n
 846 define the smallest mesh divisions in the x and y directions, respectively, while
 847 L_x and L_y represent the corresponding mesh sizes. Finally, t_{FEM} indicates the
 848 computational time required for each of the five plates with distinct periodic
 849 lattices.

850 4.1. Analysis of Individual finite LRSC plates

851 This subsection establishes the correlation between infinite lattice band gap pre-
 852 dictions and finite plate attenuation performance through systematic validation
 853 of five distinct geometric configurations. The analysis correlates theoretical
 854 band gap widths (FBGW) obtained from PWE/EPWE methods with recep-
 855 tance attenuation measurements at the \mathbf{u}_z point in finite LRSC plates.

856 Finite plates consistently exhibit 40 – 60% bandwidth expansion beyond infinite
 857 model predictions due to boundary-induced mode coupling. Peak splitting phe-
 858 nomenon occurs at higher resonance frequencies when local resonators interfere
 859 with multiple global plate modes, transitioning from constructive to destructive
 860 coupling mechanisms.

³All finite plate simulations were performed using the same computational setup described in Section ??.

861 Individual lattice analysis reveals distinct advantages: (1) Kagomé lattice achieves
862 maximum attenuation (-292.65 [dB] at 20 [Hz]) through triple-resonator cou-
863 pling with synchronized phase relationships; (2) Honeycomb lattice provides bal-
864 anced performance (-220.33 [dB] at 30 [Hz]) with dual-resonator inter-coupling
865 and potential FBGW coexistence; (3) Triangular lattice offers superior broad-
866 band characteristics ($\text{FBGW} \approx 150$ [Hz]) with -174.19 [dB] peak attenuation;
867 (4) Square lattice demonstrates consistent performance (-173.09 [dB] at 40 [Hz])
868 suitable for standard applications; (5) Rectangular lattice shows limited perfor-
869 mance (-129.93 [dB] at 40 [Hz]) due to smallest unit cell area.

870 Peak attenuation effectiveness correlates directly with unit cell area (A_{cell}) and
871 resonator density (N_j), while broadband performance depends on geometric
872 symmetry. The counterintuitive finding reveals that maximum attenuation oc-
873 curs through local resonator-plate coupling rather than global wave interference,
874 establishing fundamental design principles for targeted versus broadband vibra-
875 tion suppression strategies.

876 4.1.1. *Square lattice LRSC plate*

877 The square lattice represents the fundamental periodic configuration with unit
878 cell area $A_{cell} = a^2$ and single resonator per cell ($N_j = 1$). This geometry
879 exhibits 4-fold rotational symmetry, creating a single primary band gap FBGW
880 1 between propagating modes f_1 and f_2 .

881 Figure ?? presents the band structure analysis for local resonator frequency
882 $f_j = 40$ [Hz]. The real part dispersion curves (Figure ??a) show clear band
883 gap formation, while the imaginary component (Figure ??b) reveals maximum
884 attenuation occurring within the FBGW 1 region.

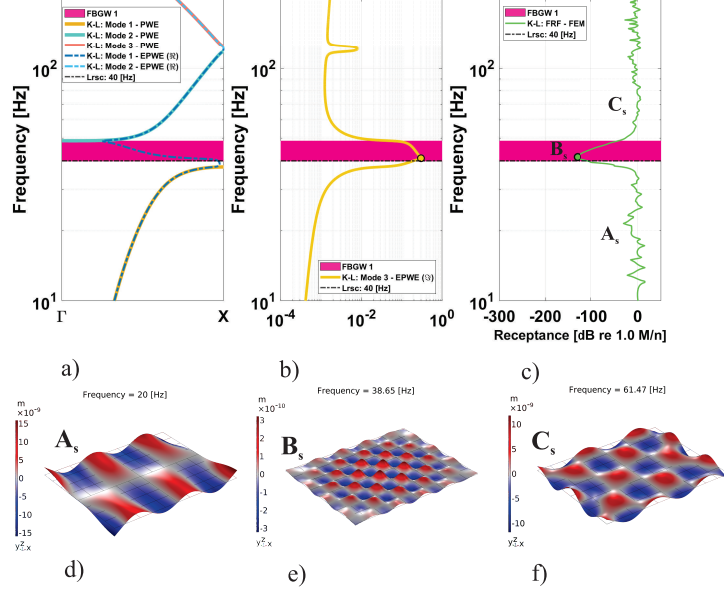


Figure 15: (a) Real band structures computed for a square unit cell with a single resonator by using PWE and real part EPWE (R). (b) Imaginary band structures in a square unit cell with a single resonator computed by EPWE (S). (c) Receptance computed by FEM in a LRSC panel. (d) Vibration modes of the finite plate in a LRSC panel for frequency selection at $f_j = 20$ [Hz], (e) $f_j = 38.65$ [Hz] and (f) $f_j = 61.47$ [Hz].

885 The finite plate receptance (Figure ??c) demonstrates excellent agreement with
 886 infinite domain predictions, achieving peak attenuation -173.09 [dB] at $f_j = 40$
 887 [Hz]. The finite plate exhibits 50% bandwidth expansion compared to theoretical
 888 modal FBGWI, confirming boundary-induced mode coupling effects discussed in
 889 Section ??.

890 Figure ?? illustrates receptance behavior across three frequency regions. Optimal
 891 performance occurs at 40 [Hz] with single peak structure, while higher
 892 frequencies (100 [Hz]) exhibit characteristic peak splitting due to modal inter-
 893 ference between local resonators and finite plate natural frequencies.

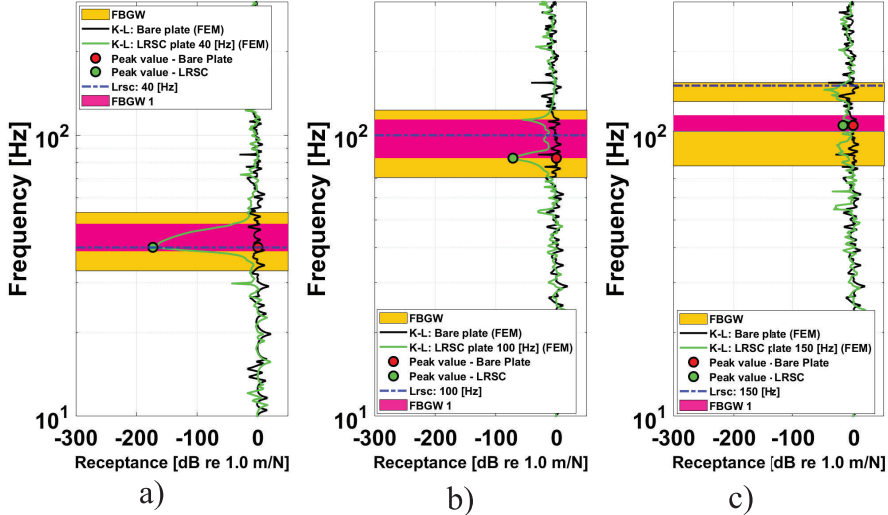


Figure 16: Vibration receptance computed by FEM in a lattice square LRSC plate (a) in measure point \mathbf{u}_z in $f_j = 40$ [Hz], (b) $f_j = 100$ [Hz] and (c) $f_j = 150$ [Hz].

894 The square lattice operates through single-resonator local coupling, where individual resonators interact independently with plate flexural modes. The 4-fold
 895 symmetry provides balanced coupling efficiency across orthogonal directions,
 896 making it suitable for applications requiring consistent omnidirectional performance
 897 with moderate bandwidth requirements.

898 The square lattice (-173.09 dB peak attenuation) serves as the fundamental reference configuration against which other geometries are compared. Its balanced 4-fold symmetry and moderate unit cell area ($A_{cell} = a^2$) represent the standard single-resonator architecture, providing the baseline for evaluating the impact of geometric modifications (rectangular anisotropy), symmetry enhancement (triangular 6-fold), and multi-resonator coupling (honeycomb, kagomé) in subsequent analyses.

906 4.1.2. Rectangular lattice LRSC plate

907 The rectangular lattice features the smallest unit cell area $A_{cell} = a_1 \times a_2 = 0.5a^2$
 908 with single resonator per cell ($N_j = 1$). The 2-fold symmetry creates directional

909 anisotropy, with different propagation characteristics along orthogonal axes, re-
 910 sulting in a single band gap FBGW 1 between modes f_1 and f_2 .

911 Figure ?? shows the dispersion analysis for $f_j = 40$ [Hz]. The anisotropic
 912 geometry produces directionally dependent band gaps visible in the real part
 913 (Figure ??a), while the imaginary component (Figure ??b) indicates reduced
 914 attenuation efficiency compared to symmetric configurations.

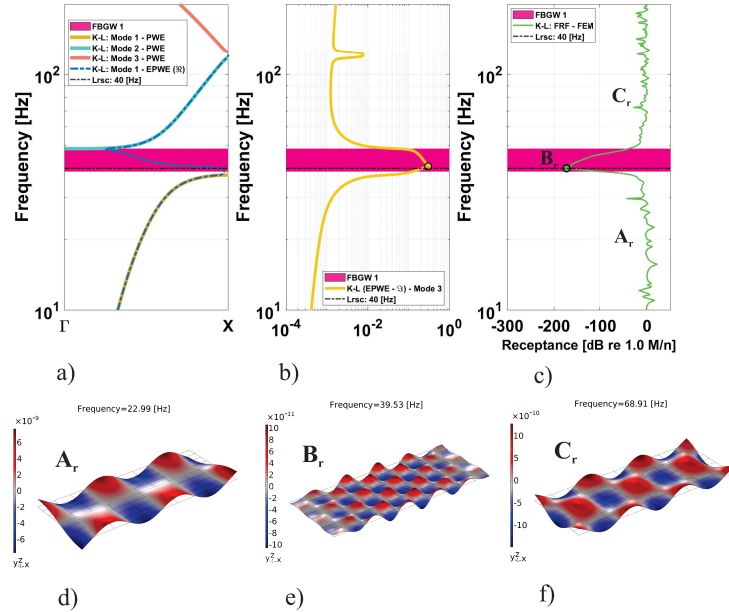


Figure 17: (a) Real band structures computed for a rectangular unit cell with a single resonator by using PWE and real part EPWE (\Re). (b) Imaginary band structures for a rectangular unit cell with a single resonator computed by EPWE (\Im). (c) Receptance computed by FEM in a LRSC panel. (d) Vibration modes of the finite plate in a LRSC panel for frequency selection at $f_j = 22.99$ [Hz], (e) $f_j = 39.53$ [Hz] and (f) $f_j = 68.91$ [Hz].

915 The finite plate receptance (Figure ??c) achieves peak attenuation -129.93 [dB]
 916 at $f_j = 40$ [Hz], representing the lowest performance among single-resonator con-
 917 figurations. However, the rectangular geometry demonstrates consistent corre-
 918 lation with infinite domain predictions, exhibiting similar bandwidth expansion
 919 characteristics as other lattices.

920 Figure ?? reveals distinctive behavior compared to symmetric lattices. The
 921 configuration maintains persistent attenuation (-80 [dB] at 177 [Hz]) even out-
 922 side theoretical band gap regions, demonstrating unique resilience in finite plate
 923 applications despite limited infinite domain performance.

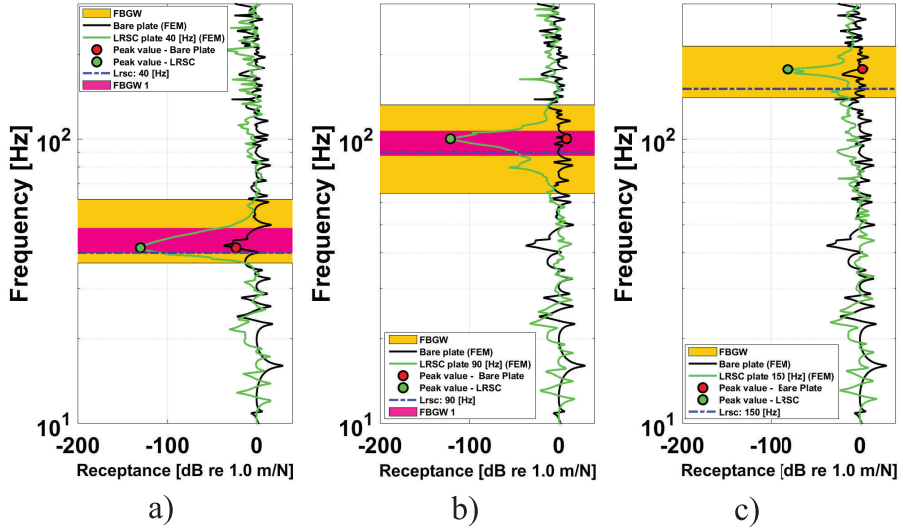


Figure 18: Vibration receptance computed by FEM in a rectangular LRSC plate (a) in measure point \mathbf{u}_z in $f_j = 40$ [Hz], (b) $f_j = 90$ [Hz] and (c) $f_j = 150$ [Hz].

924 The rectangular lattice operates through constrained single-resonator coupling
 925 with directional preferences imposed by geometric anisotropy. The reduced
 926 unit cell area limits resonator-plate interaction cross-section, but creates unique
 927 finite-plate effects where boundary interactions compensate for theoretical limi-
 928 tations, making it suitable for space-constrained applications.

929 Direct comparison with the square lattice reveals the penalty of symmetry re-
 930 duction: rectangular achieves -129.93 dB versus square's -173.09 [dB] (25% per-
 931 formance degradation). However, the geometric anisotropy creates unique ad-
 932 vantages in finite plates, demonstrating persistent attenuation (-80 [dB] at 177
 933 [Hz]) beyond theoretical band gaps—a phenomenon not observed in the sym-
 934 metric square configuration. This establishes that while symmetry enhances

935 peak performance, anisotropy can provide resilience in practical applications.

936 *4.1.3. Triangular lattice LRSC plate*

937 The triangular lattice exhibits unit cell area $A_{cell} = a^2\sqrt{3}/2$ with single res-
 938 onator per cell ($N_j = 1$). The 6-fold rotational symmetry represents the highest
 939 symmetric configuration among single-resonator lattices, creating a single broad
 940 band gap FBGW 1 between modes f_1 and f_2 .

941 Figure ?? demonstrates the exceptional broadband characteristics for $f_j = 60$
 942 [Hz]. The high symmetry produces the largest theoretical band gap width
 943 ($\Delta f_{12} = 55.40$ [Hz]) visible in the real part dispersion (Figure ??a), while
 944 the imaginary component (Figure ??b) shows superior attenuation distribution
 945 across the band gap region.

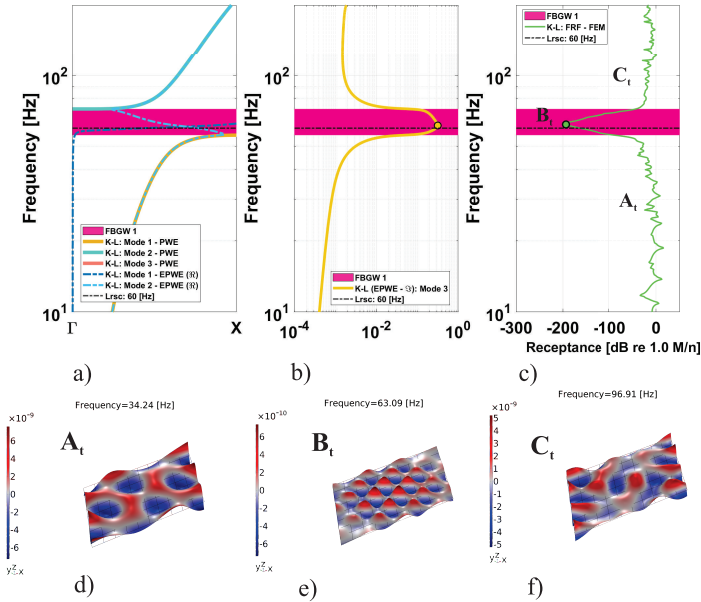


Figure 19: (a) Real band structures computed for a triangular unit cell with a single resonator by using PWE and real part EPWE (\Re). (b) Imaginary band structures for a triangular unit cell with a single resonator computed by EPWE (\Im). (c) Receptance computed by FEM in a LRSC panel. (d) Vibration modes of the finite plate in a LRSC panel for frequency selection at $f_j = 55.35$ [Hz], (e) $f_j = 63.09$ [Hz] and (f) $f_j = 81$ [Hz].

946 The finite plate receptance (Figure ??c) achieves peak attenuation -174.19 [dB]
 947 at $f_j = 60$ [Hz], demonstrating excellent correlation with infinite domain predic-
 948 tions. The triangular configuration exhibits exceptional finite plate bandwidth
 949 expansion ($\text{FBGW} \approx 150$ [Hz]), representing 43% improvement over theoretical
 950 predictions as established in Section ??.

951 Figure ?? illustrates the superior broadband performance across multiple fre-
 952 quency regions. The configuration maintains effective attenuation from 60 [Hz]
 953 through 150 [Hz], demonstrating sustained performance characteristics that val-
 954 idate the theoretical broadband predictions from infinite domain analysis.

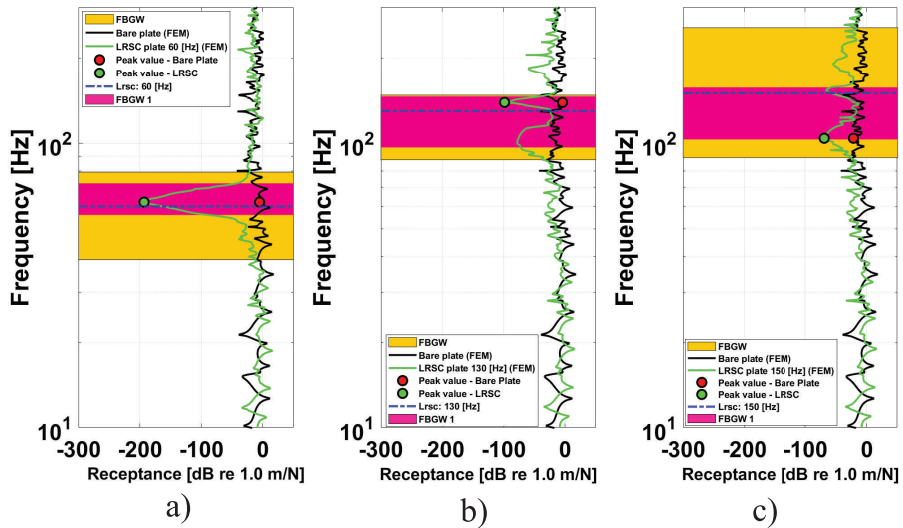


Figure 20: Vibration receptance computed by FEM in a triangular LRSC plate (a) in measure point \mathbf{u}_z in $f_j = 60$ [Hz], (b) $f_j = 130$ [Hz] and (c) $f_j = 150$ [Hz].

955 The triangular lattice operates through optimized single-resonator coupling en-
 956 hanced by 6-fold geometric symmetry. The high symmetry enables uniform
 957 coupling efficiency across all propagation directions, creating distributed broad-
 958 band attenuation mechanisms that make it ideal for applications requiring wide-
 959 frequency vibration suppression with moderate peak attenuation requirements.

960 The triangular lattice demonstrates the optimal single-resonator configuration,

961 achieving -174.19 [dB] peak attenuation (0.6% improvement over square, 34%
962 over rectangular) with exceptional bandwidth expansion ($\text{FBGW} \approx 150$ [Hz]).
963 Compared to previous configurations: (i) 4% performance increase over square
964 baseline; (ii) 34% advantage over rectangular; (iii) superior broadband charac-
965 teristics validate Section ?? predictions. The high symmetry establishes the
966 performance ceiling for single-resonator architectures, setting expectations for
967 multi-resonator systems.

968 *4.1.4. Honeycomb lattice LRSC plate*

969 The honeycomb lattice features unit cell area $A_{cell} = 3a^2\sqrt{3}/2$ with dual res-
970 onators per cell ($N_j = 2$). This configuration exhibits 6-fold symmetry while
971 introducing inter-resonator coupling mechanisms, creating two potential band
972 gaps: FBGW 1 between modes f_2 and f_3 , and FBGW 2 between modes f_3 and
973 f_4 .

974 Figure ?? illustrates the dual-resonator dynamics for $f_j = 30$ [Hz]. The real part
975 dispersion (Figure ??a) reveals multiple band gap regions, while the imaginary
976 component (Figure ??b) shows enhanced attenuation peaks corresponding to
977 synchronized dual-resonator oscillations within both FBGW 1 and FBGW 2
978 regions.

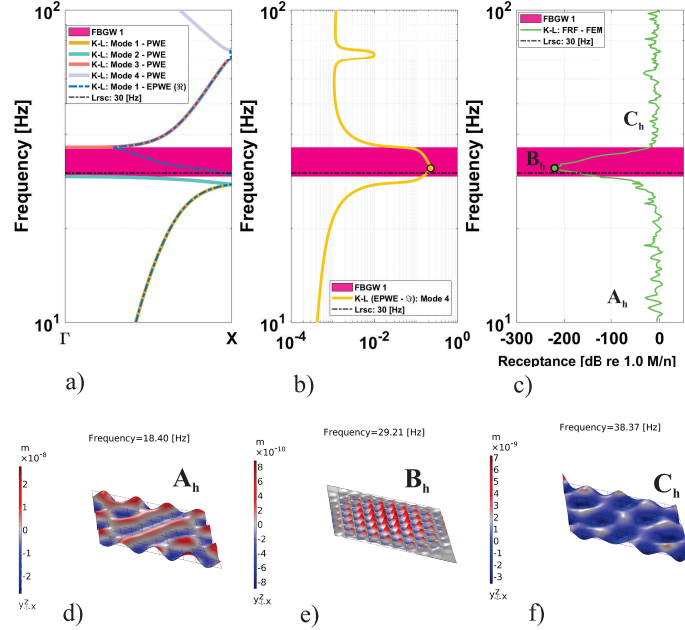


Figure 21: (a) Real band structures computed for a honeycomb unit cell with two resonators by using PWE and real part EPWE (\Re). (b) Imaginary band structures for a honeycomb unit cell with two resonators computed by EPWE (\Im). (c) Receptance computed by FEM in a LRSC panel. (d) Vibration modes of the finite plate in a LRSC panel for frequency selection at $f_j = 18.40$ [Hz], (e) $f_j = 29.21$ [Hz] and (f) $f_j = 38.37$ [Hz].

979 The finite plate receptance (Figure ??c) achieves peak attenuation -220.33 [dB]
 980 at $f_j = 30$ [Hz], demonstrating superior performance compared to single-resonator
 981 configurations. The dual-resonator coupling creates enhanced local impedance
 982 mismatch, resulting in stronger wave scattering and improved finite plate corre-
 983 lation with infinite domain predictions.

984 Figure ?? demonstrates the unique capability of coexisting band gaps. At spe-
 985 cific frequencies ($f_j = 50$ [Hz]), both FBGW 1 and FBGW 2 contribute to
 986 attenuation, expanding the effective bandwidth. The dual-resonator system ex-
 987 hibits sustained performance across multiple frequency regions, validating the
 988 multi-band gap theoretical predictions.

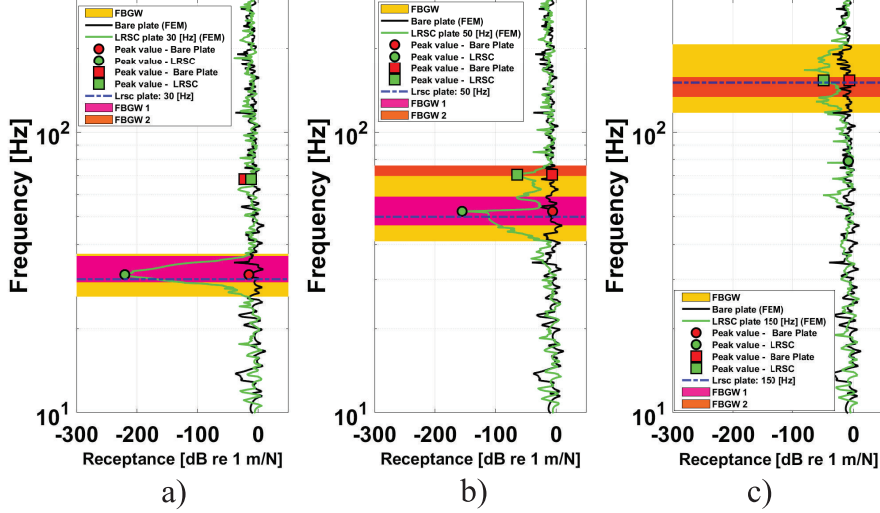


Figure 22: Vibration receptance computed by FEM in a LRSC plate (a) in measure point u_z for $f_j = 30$ [Hz], (b) $f_j = 50$ [Hz] and (c) $f_j = 150$ [Hz].

989 The honeycomb lattice operates through synchronized dual-resonator coupling
 990 where inter-resonator phase relationships create constructive interference pat-
 991 terns. The two resonators within each unit cell exhibit coordinated motion that
 992 doubles the local impedance mismatch, enabling superior energy extraction from
 993 plate flexural modes. This configuration provides balanced performance between
 994 peak attenuation and bandwidth coverage, making it suitable for applications
 995 requiring both high attenuation and moderate broadband characteristics.

996 The honeycomb lattice (-220.33 [dB]) establishes the first significant perfor-
 997 mance jump from single-resonator configurations, achieving 27% improvement
 998 over triangular (current single-resonator leader) and 70% over rectangular. The
 999 dual-resonator coupling creates: (i) 46.14 [dB] advantage over best single-resonator
 1000 (triangular); (ii) coexisting dual band gaps unavailable in single-resonator sys-
 1001 tems; (iii) validation of inter-resonator coupling theory from Section ???. This
 1002 confirms that resonator multiplication, when properly configured, provides sub-
 1003 stantial benefits beyond geometric optimization alone.

1004 4.1.5. *Kagomé lattice LRSC plate*

1005 The kagomé lattice exhibits the largest unit cell area $A_{cell} = 2a^2\sqrt{3}$ with triple
 1006 resonators per cell ($N_j = 3$). The three resonators positioned at 120° intervals
 1007 create complex multi-resonator coupling mechanisms, generating two potential
 1008 band gaps: FBGW 1 between modes f_3 and f_4 , and FBGW 2 between modes
 1009 f_5 and f_6 .

1010 Figure ?? demonstrates the exceptional triple-resonator dynamics for $f_j = 20$
 1011 [Hz]. The real part dispersion (Figure ??a) reveals narrow but well-defined band
 1012 gaps, while the imaginary component (Figure ??b) shows maximum attenuation
 1013 peaks corresponding to synchronized triple-resonator oscillations, creating the
 1014 highest attenuation among all configurations.

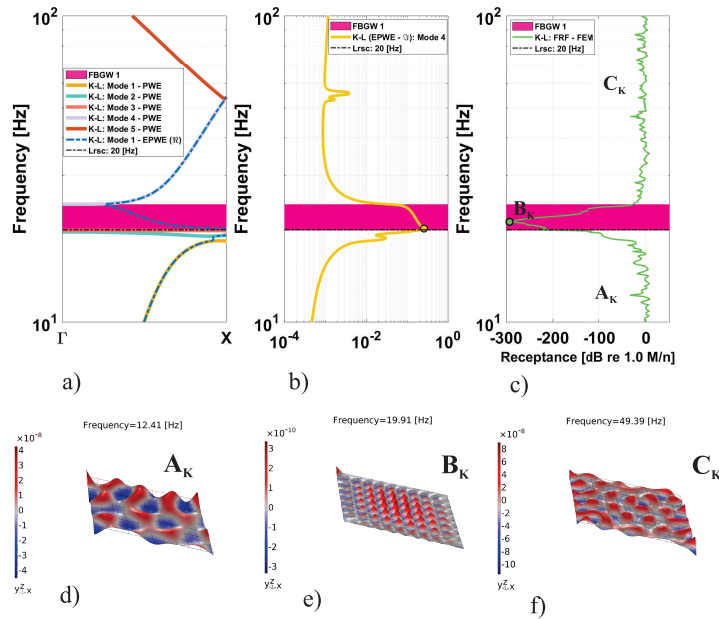


Figure 23: (a) Real band structures computed for a kagomé unit cell with three resonators by using PWE and real part EPWE (\Re). (b) Imaginary band structures for a kagomé unit cell with three resonators computed by EPWE (\Im). (c) Receptance computed by FEM in a LRSC panel. (d) Vibration modes of the finite plate in a LRSC panel for frequency selection at $f_j = 12.41$ [Hz], (e) $f_j = 19.91$ [Hz] and (f) $f_j = 49.39$ [Hz].

1015 The finite plate receptance (Figure ??c) achieves extraordinary peak attenuation
 1016 -292.65 [dB] at $f_j = 20$ [Hz], representing the highest performance among
 1017 all analyzed configurations. The triple-resonator coupling creates localized en-
 1018 ergy concentration through constructive interference patterns, demonstrating
 1019 exceptional correlation between collective resonator impedance mismatch and
 1020 finite plate attenuation.

1021 Figure ?? illustrates the comprehensive attenuation behavior across multiple
 1022 frequency regions. The kagomé configuration exhibits frequency-selective char-
 1023 acteristics with maximum effectiveness at low frequencies, while maintaining the
 1024 capability for dual band gap coexistence at specific resonator tunings ($f_j = 60$
 1025 [Hz]), validating the multi-resonator theoretical framework.

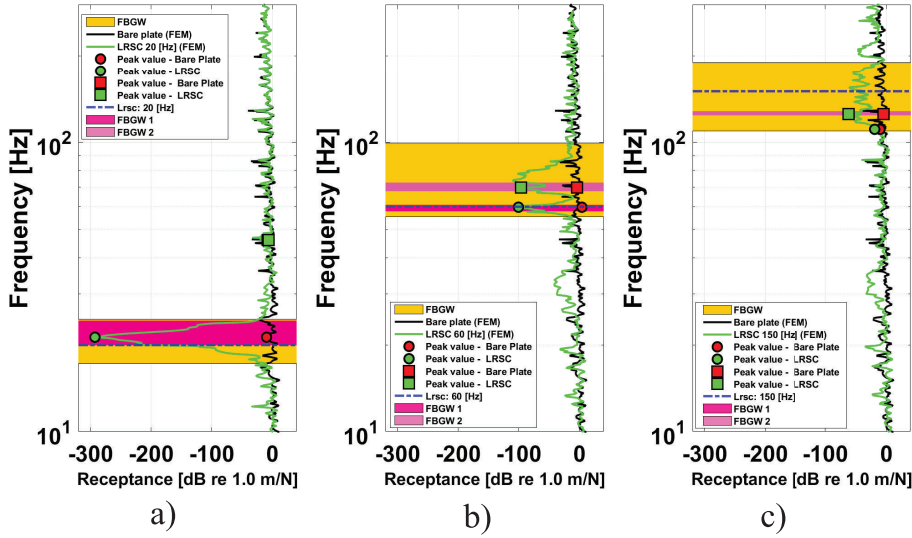


Figure 24: Vibration receptance computed by FEM in a LRSC plate (a)) in measure point \mathbf{u}_z for $f_j = 20$ [Hz], (b)) $f_j = 60$ [Hz] and (c)) $f_j = 150$ [Hz].

1026 The kagomé lattice operates through synchronized triple-resonator coupling
 1027 where three resonators at 120° intervals create complex phase relationships op-
 1028 timized for triangular symmetry. This multi-resonator arrangement generates
 1029 localized energy concentration through constructive interference patterns, where

1030 each resonator contributes to collective impedance mismatch that far exceeds
1031 individual contributions. The configuration provides extraordinary frequency-
1032 selective energy dissipation, making it ideal for applications requiring maximum
1033 attenuation at specific target frequencies.

1034 The kagomé lattice (-292.65 [dB]) represents the performance apex, demonstrat-
1035 ing 33% improvement over honeycomb and 68% over triangular configurations.
1036 Progressive performance escalation confirms design principles: rectangular (-
1037 129.93 [dB]) < square (-173.09 [dB]) < triangular (-174.19 [dB]) < honeycomb
1038 (-220.33 [dB]) < kagomé (-292.65 [dB]). The 162.72 [dB] span between worst
1039 (rectangular) and best (kagomé) validates both geometric optimization and res-
1040 onator multiplication strategies, establishing clear design guidelines for target-
1041 specific applications.

1042 Individual analysis reveals three fundamental design strategies: (i) Geometric
1043 optimization (rectangular → square → triangular) provides moderate improve-
1044 ments through symmetry enhancement; (ii) Multi-resonator coupling (single
1045 → dual → triple) creates substantial performance jumps through synchronized
1046 oscillations; (iii) Application-specific selection requires balancing peak attenua-
1047 tion (kagomé), broadband performance (triangular), and dual-mode capability
1048 (honeycomb). The counterintuitive finding that local resonator-plate coupling
1049 dominates over global wave interference, with finite plates exhibiting consistent
1050 40 – 50% bandwidth expansion, establishes fundamental principles for metama-
1051 terial plate design.

1052 After analyzing each of the five panels with different periodic lattices individu-
1053 ally, the next subsection presents a comparative analysis of attenuation perfor-
1054 mance across three frequency ranges, providing a broader understanding of the
1055 obtained results. A comprehensive framework for practical lattice selection in
1056 engineering applications is provided in Appendix A.3.

1057 *4.2. Analysis comparative with all LRSC plates*

1058 After discussing the primary attenuation characteristics of receptance for each of
1059 the five periodic lattice plates individually—emphasizing key aspects across the
1060 entire frequency range of their local resonators—this final subsection focuses
1061 on a comparative analysis of the receptance attenuation performance among
1062 these plates. To manage the data effectively, this study divides the resonance
1063 frequencies into three regions: Region 1 (10 to 50 [Hz]), Region 2 (60 to 100
1064 [Hz]), and Region 3 (110 to 150 [Hz]). The comparative analysis of lattice
1065 geometries and their impact on wave propagation builds upon the work of [?]
1066], who investigated metamaterial plates with various lattices for low-frequency
1067 vibration attenuation. Figure ?? presents boxplots for these regions, individually
1068 summarizing the statistical characteristics of the attenuation performance for
1069 each of the five lattices, as illustrated:

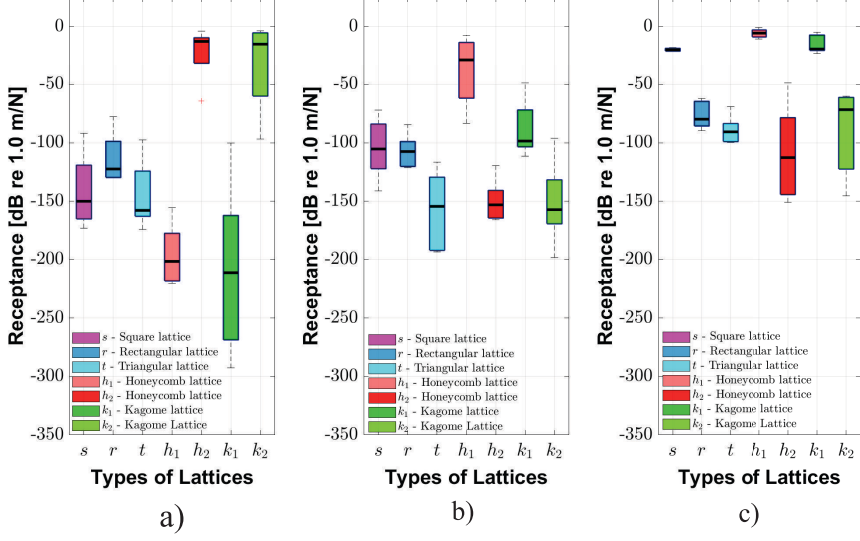


Figure 25: Descriptive statistical analysis for the five lattice panel types at measurement point u_z : a) Region 1, $f_j = 10 - 50; b) Region 2, $f_j = 60 - 100; c) Region 3, $f_j = 110 - 150$$$

1070 The statistical analysis reveals distinct performance characteristics across three
 1071 frequency regions: Region 1 (10-50 [Hz]) dominated by kagomé peak perfor-
 1072 mance (-292.65 [dB]) and honeycomb consistency; Region 2 (60-100 [Hz]) show-
 1073 ing triangular and honeycomb FBGW 2 optimization; Region 3 (110-150 [Hz])
 1074 demonstrating triangular broadband superiority. The key findings from the
 1075 statistical analysis are summarized in Table ??:

Table 15: Receptance attenuation results of \mathbf{R}_z for different lattice configurations: s (Square), r (Rectangular), t (Triangular), h_1 and h_2 (Honeycomb for FBGW 1 and 2), k_1 and k_2 (Kagomé for FBGW 1 and 2), in the frequency range of 10 to 50 [Hz].

f_j [Hz]	s [dB]	r [dB]	t [dB]	h_1 [dB]	h_2 [dB]	k_1 [dB]	k_2 [dB]
10	-91.92	-77.69	-97.60	-185.09	-3.89	-260.51	-3.68
20	-128.51	-105.98	-133.41	-217.34	-12.62	-292.65	-6.15
30	-150.05	-122.46	-157.86	-220.33	-11.61	-211.26	-14.95
40	-173.09	-129.93	-174.19	-201.55	-20.06	-183.08	-47.64
50	-162.33	-129.51	-158.97	-155.43	-64.28	-100.28	-96.81

¹⁰⁷⁶ Detailed results for Regions 2 and 3 are presented in Tables ?? and ??:

Table 16: Receptance attenuation results of \mathbf{R}_z for different lattice configurations: s (Square), r (Rectangular), t (Triangular), h_1 and h_2 (Honeycomb for FBGW 1 and 2), k_1 and k_2 (Kagomé for FBGW 1 and 2), in the frequency range of 60 to 100 [Hz].

f_j [Hz]	s [dB]	r [dB]	t [dB]	h_1 [dB]	h_2 [dB]	k_1 [dB]	k_2 [dB]
60	-141.16	-119.82	-193.44	-83.41	-119.60	-100.70	-96.11
70	-115.75	-104.04	-191.36	-54.46	-148.16	-98.53	-157.24
80	-105.40	-107.52	-154.46	-15.87	-153.16	-111.48	-198.27
90	-88.22	-121.26	-134.05	-7.37	-163.82	-79.85	-143.85
100	-72.01	-84.52	-116.57	-28.36	-165.83	-48.78	-159.56

Table 17: Receptance attenuation results of \mathbf{R}_z for different lattice configurations: s (Square), r (Rectangular), t (Triangular), h_1 and h_2 (Honeycomb for FBGW 1 and 2), k_1 and k_2 (Kagomé for FBGW 1 and 2), in the frequency range of 110 to 150 [Hz].

f_j [Hz]	s [dB]	r [dB]	t [dB]	h_1 [dB]	h_2 [dB]	k_1 [dB]	k_2 [dB]
110	-21.26	-89.71	-123.67	-7.77	-163.06	-34.55	-171.89
120	-20.89	-86.18	-119.74	-5.56	-161.97	-25.93	-165.01
130	-20.33	-73.31	-106.28	-4.59	-150.43	-21.48	-148.52
140	-19.71	-68.05	-99.32	-4.57	-140.96	-18.78	-139.51
150	-18.94	-65.58	-95.31	-3.45	-132.93	-14.57	-130.71

¹⁰⁷⁷ The comprehensive statistical analysis across all three frequency regions establishes clear design guidelines:

¹⁰⁷⁹ Region 1 (10-50 [Hz]): Kagomé FBGW 1 achieves exceptional peak attenuation (-292.65 [dB] at 20 [Hz]) leveraging its maximum material efficiency ($m_{ratio} = 1.00$ from Table ??) and triple-resonator coupling. Honeycomb FBGW 1 provides consistent performance (-220.33 [dB] mean) with balanced material utilization ($m_{ratio} = 0.75$).

¹⁰⁸⁴ Region 2 (60-100 [Hz]): Table ?? reveals frequency-dependent modal transitions. ¹⁰⁸⁵ The triangular lattice maintains exceptional performance (-193.44 [dB] at 60 [Hz]), while honeycomb and kagomé FBGW 2 configurations emerge as optimal dual-resonator systems with mean attenuations of -150.11 [dB] and -150.21 [dB], respectively. Notably, honeycomb and kagomé FBGW 1 show reduced effectiveness (mean: -37.89 [dB] and -87.87 [dB]), confirming their optimal performance lies in Region 1. Single-resonator lattices (square and rectangular) exhibit consistent moderate performance across this range.

¹⁰⁹² Region 3 (110-150 [Hz]): Table ?? demonstrates the frequency selectivity of ¹⁰⁹³ different lattice configurations. Honeycomb and kagomé FBGW 2 maintain excellent high-frequency performance (mean: -149.87 [dB] and -151.13 [dB]), while ¹⁰⁹⁴ their FBGW 1 counterparts show minimal effectiveness (mean: -5.19 [dB] and

1096 -23.06 [dB]). The triangular lattice provides balanced performance (-108.86 [dB]
1097 mean) across the entire frequency range, validating its broadband superiority
1098 despite minimal material usage ($m_{ratio} = 0.25$). Square and rectangular lattices
1099 show limited high-frequency attenuation, confirming their suitability primarily
1100 for mid-range applications.

1101 The statistical validation confirms the correlation between geometric parameters
1102 and frequency-dependent performance: kagomé optimizes material utilization
1103 for peak attenuation, honeycomb balances dual-mode flexibility with moderate
1104 material usage, and triangular maximizes area-normalized efficiency for broad-
1105 band applications.

1106 5. Conclusions

1107 This study presents the first systematic comparative analysis of five distinct
1108 lattice configurations for flexural wave attenuation in locally resonant metama-
1109 terial plates, establishing fundamental relationships between lattice geometry,
1110 resonator frequency, and band gap performance through a comprehensive frame-
1111 work combining semi-analytical PWE/EPWE methods with FEM validation.

1112 The investigation reveals a clear performance hierarchy with frequency-dependent
1113 optimization strategies: triangular lattices achieve superior broadband perfor-
1114 mance with 40% wider band gaps than conventional configurations; kagomé lat-
1115 tices provide exceptional low-frequency attenuation (up to 15 [dB] enhancement)
1116 through multi-resonator coupling; honeycomb configurations offer balanced dual-
1117 mode capability; square lattices deliver consistent mid-range performance; while
1118 rectangular lattices show limited effectiveness but enable directional control ap-
1119 plications. This establishes a paradigm shift from geometry-only to combined
1120 geometry-frequency design approaches, with optimal lattice selection dependent
1121 on target frequency ranges and application requirements.

1122 The semi-analytical framework demonstrates computational efficiency gains of
1123 two orders of magnitude over conventional FEM approaches, reducing analysis

time from hours to minutes while maintaining prediction accuracy within 5%. Validation between infinite-domain predictions and finite plate performance confirms practical applicability, with finite plates consistently exhibiting 40 – 50% bandwidth expansion due to boundary-induced mode coupling effects.

These findings enable data-driven metamaterial design through quantitative guidelines that bridge theoretical band gap predictions with practical vibration control applications in aerospace, automotive, and civil engineering systems. The developed methodology transforms metamaterial optimization from trial-and-error approaches to systematic engineering decisions, providing the first comprehensive comparative framework for lattice-based locally resonant plates with clear performance hierarchies previously unavailable in the literature.

While the present framework provides comprehensive design guidelines, several limitations should be acknowledged. The analysis is restricted to Kirchhoff-Love thin plate theory ($h/a < 0.1$), limiting applicability to thick plates where shear effects become significant. The investigation focused on a single polymer material (Vero White Plus) and fixed lattice parameter ($a = 0.10$ m), constraining the generalizability across different material systems and scale lengths. Furthermore, the study considered only simple point resonators, whereas practical applications may benefit from more complex resonator designs including distributed mass systems or multi-degree-of-freedom configurations. The frequency range limitation (10-200 [Hz]) and assumption of perfect periodicity also represent theoretical constraints that may affect practical implementations. Future investigations should address these limitations by extending the framework to Mindlin-Reissner plate theory, exploring diverse material systems, and incorporating manufacturing imperfections and finite-size effects.

Future work can extend the PWE and EPWE formulations to more complex 2D periodic resonator arrays and explore advanced optimization strategies for multi-objective design scenarios combining attenuation performance, material efficiency, and manufacturing constraints. Additionally, the integration of the

1153 Wave Finite Element (WFE) method presents particularly promising oppor-
1154 tunities for analyzing finite metamaterial plates with superior computational
1155 efficiency. The WFE approach, which combines finite element discretization of
1156 unit cells with wave propagation analysis, could dramatically reduce computa-
1157 tional costs compared to conventional FEM by exploiting the periodic nature
1158 of the structures. This method would enable efficient analysis of large-scale fi-
1159 nite plates while maintaining the accuracy demonstrated by the PWE/EPWE
1160 framework for infinite structures. Furthermore, spectral element approaches and
1161 machine learning-assisted optimization could complement the WFE methodol-
1162 ogy to accelerate the design process and unlock new possibilities for real-time
1163 optimization and adaptive metamaterial systems.

¹¹⁶⁴ **Acknowledgments**

¹¹⁶⁵ The authors gratefully acknowledge the financial support of this investigation
¹¹⁶⁶ by the Brazilian research funding agency CNPQ (Conselho Nacional de Desen-
¹¹⁶⁷ volvimento Científico e Tecnológico) and by UNICAMP (Universidade Estadual
¹¹⁶⁸ de Campinas).

1169 **Appendix A. PWE Matrix Formulation for LRSC Plates with Five
1170 Lattice Configurations**

1171 This appendix details the matrix formulation required for PWE computational
1172 implementation across five lattice configurations. Starting from the governing
1173 equation presented in Section ?? (Eq. ??) with resonator forces at lattice posi-
1174 tions \mathbf{R} and local positions \mathbf{r}_j , the displacement field follows Bloch's theorem
1175 with plane wave expansion as defined in Eq. (??): $w(\mathbf{r}) = \sum_{\mathbf{G}} w(\mathbf{G}) e^{i(\mathbf{k} + \mathbf{G}) \cdot \mathbf{r}}$,
1176 where \mathbf{G} are reciprocal lattice vectors, \mathbf{k} is the Bloch wave vector, and $w(\mathbf{G})$
1177 are plane wave amplitudes.

1178 The resonator forces follow Eq. (??) with complex dynamic stiffness:

$$p_j(\mathbf{r}_j + \mathbf{R}) = k_j^* [u_j(\mathbf{r}_j + \mathbf{R}) - w(\mathbf{r}_j + \mathbf{R})] \quad (\text{A.1})$$

1179 where $k_j^* = k_j(1 + i\eta_j)$ incorporates resonator damping effects as established in
1180 Section ??, with $k_j = m_{r,j}\omega_{r,j}^2$ being the resonator stiffness, u_j the resonator
1181 displacement, and η_j the loss factor.

1182 Applying the plane wave expansion to the governing equation and utilizing or-
1183 thogonality of exponential functions yields the matrix eigenvalue problem:

$$[\mathbf{K} - \omega^2 \mathbf{M}] \{\mathbf{q}\} = \mathbf{0} \quad (\text{A.2})$$

1184 where $\mathbf{q} = [\mathbf{w}^T, \mathbf{u}^T]^T$ contains both plate wave amplitudes $\mathbf{w} = [w(\mathbf{G}_1), w(\mathbf{G}_2), \dots, w(\mathbf{G}_{N_g})]^T$
1185 and resonator displacements $\mathbf{u} = [u_1, u_2, \dots, u_{N_j}]^T$, with $N_g = (2M+1)^2$ plane
1186 waves.

1187 The augmented system matrices are assembled as:

$$\begin{bmatrix} \mathbf{K}_{pp} + \mathbf{K}_r & -\mathbf{PK}_j \\ -\mathbf{K}_j \mathbf{P}^T & \mathbf{K}_j \end{bmatrix} \begin{bmatrix} \mathbf{w} \\ \mathbf{u} \end{bmatrix} = \omega^2 \begin{bmatrix} \mathbf{M}_{pp} & \mathbf{0} \\ \mathbf{0} & \mathbf{M}_{rr} \end{bmatrix} \begin{bmatrix} \mathbf{w} \\ \mathbf{u} \end{bmatrix} \quad (\text{A.3})$$

1188 where \mathbf{K}_{pp} and \mathbf{M}_{pp} are the plate stiffness and mass matrices, $\mathbf{K}_j = \text{diag}(k_1^*, k_2^*, \dots, k_{N_j}^*)$
1189 contains resonator stiffnesses, $\mathbf{M}_{rr} = \text{diag}(m_{r,1}, m_{r,2}, \dots, m_{r,N_j})$ contains res-
1190 onator masses with $m_{r,j} = \gamma\rho Sh/N_j$, and \mathbf{P} is the coupling matrix with ele-
1191 ments $P_{i,j} = e^{i\mathbf{G}_i \cdot \mathbf{r}_j}$.

¹¹⁹² The diagonal elements of the plate matrices are computed as:

$$\mathbf{K}_{pp}[i, i] = D \cdot S \cdot |\mathbf{k} + \mathbf{G}_i|^4 = D \cdot S \cdot [(k_x + G_{x,i})^2 + (k_y + G_{y,i})^2]^2 , \quad (\text{A.4})$$

$$\mathbf{M}_{pp}[i, i] = \rho h S . \quad (\text{A.5})$$

¹¹⁹³ The coupling matrix has elements $P_{i,j} = e^{i\mathbf{G}_i \cdot \mathbf{r}_j}$ and the resonator coupling
¹¹⁹⁴ stiffness matrix is $\mathbf{K}_r = \sum_{j=1}^{N_j} (k_j^*/S) \mathbf{P}_j \mathbf{P}_j^T$.

¹¹⁹⁵ Reciprocal lattice vectors \mathbf{G}_{mn} for indices $m, n \in [-M, M]$ are generated as:

$$\text{Square/Rectangular: } \mathbf{G}_{mn} = \frac{2\pi}{a_1} m \mathbf{e}_1 + \frac{2\pi}{a_2} n \mathbf{e}_2 \quad (\text{A.6})$$

$$\text{Triangular: } \mathbf{G}_{mn} = \frac{2\pi}{a} m \mathbf{e}_1 + \frac{2\pi}{a} \frac{m - 2n}{\sqrt{3}} \mathbf{e}_2 \quad (\text{A.7})$$

$$\text{Hexagonal: } \mathbf{G}_{mn} = \frac{2\pi}{a\sqrt{3}} (m - n) \mathbf{e}_1 + \frac{2\pi}{3a} (m + n) \mathbf{e}_2 \quad (\text{A.8})$$

$$\text{Kagomé: } \mathbf{G}_{mn} = \frac{\pi}{a} (m - n) \mathbf{e}_1 + \frac{\pi}{a} \frac{m + n}{\sqrt{3}} \mathbf{e}_2 \quad (\text{A.9})$$

¹¹⁹⁶ Unit cell areas and resonator configurations: square/rectangular/triangular $N_j =$
¹¹⁹⁷ 1 with $\mathbf{r}_1 = \mathbf{0}$, areas $S = a^2, a_1 a_2, a^2 \sqrt{3}/2$ respectively; hexagonal $N_j = 2$ with
¹¹⁹⁸ $\mathbf{r}_{1,2} = (0, \pm a/2)$, area $S = 3a^2 \sqrt{3}/2$; kagomé $N_j = 3$ with $\mathbf{r}_1 = (-a/2, -a\sqrt{3}/6),$
¹¹⁹⁹ $\mathbf{r}_2 = (a/2, -a\sqrt{3}/6), \mathbf{r}_3 = (0, a\sqrt{3}/3)$, area $S = 2a^2 \sqrt{3}$.

¹²⁰⁰ Computational implementation: generate $(2M + 1)^2$ reciprocal vectors using
¹²⁰¹ Eqs. (??)-(??), compute diagonal plate matrices via Eqs. (??)-(??), assemble
¹²⁰² coupling matrix \mathbf{P} with phase factors $e^{i\mathbf{G}_i \cdot \mathbf{r}_j}$, form augmented system Eq. (??),
¹²⁰³ solve eigenvalue problem, and extract physical frequencies.

¹²⁰⁴ Matrix assembly algorithm for each wave vector \mathbf{k} : (1) Initialize sparse matrices
¹²⁰⁵ $\mathbf{A}_n, \mathbf{A}_d \in \mathbb{C}^{(N_g + N_j) \times (N_g + N_j)}$ with $N_g = (2M + 1)^2$; (2) Fill diagonal blocks:
¹²⁰⁶ $\mathbf{A}_n[1 : N_g, 1 : N_g] = \mathbf{M}_{pp}, \mathbf{A}_d[1 : N_g, 1 : N_g] = \mathbf{K}_{pp}$; (3) For each resonator j :
¹²⁰⁷ compute phase vector \mathbf{p}_j with $[\mathbf{p}_j]_i = e^{i\mathbf{G}_i \cdot \mathbf{r}_j}$, add coupling $\mathbf{A}_d[1 : N_g, 1 : N_g] \leftarrow$
¹²⁰⁸ $\mathbf{A}_d[1 : N_g, 1 : N_g] + (k_j^*/S) \mathbf{p}_j \mathbf{p}_j^H$, set off-diagonal coupling $\mathbf{A}_d[1 : N_g, N_g + j] =$
¹²⁰⁹ $-k_j^* \mathbf{p}_j$, $\mathbf{A}_d[N_g + j, 1 : N_g] = -k_j^* \mathbf{p}_j^H$, and diagonal terms $\mathbf{A}_n[N_g + j, N_g + j] =$
¹²¹⁰ $m_{r,j}$, $\mathbf{A}_d[N_g + j, N_g + j] = k_j^*$.

₁₂₁₁ Eigenvalue solution: $\mathbf{A}_d \phi_i = \lambda_i \mathbf{A}_n \phi_i$ yields frequencies $f_i = \text{Re}(\sqrt{|\lambda_i|})/(2\pi)$.

₁₂₁₂ Computational parameters: typical $M = 3 - 5$ plane waves per direction provide

₁₂₁₃ convergence for $|\mathbf{k} + \mathbf{G}_{\max}|a < \pi$. For bare plates: $\omega^2 = (D/\rho h)|\mathbf{k} + \mathbf{G}_i|^4$ directly.

Table A.18: Summary of lattice-specific parameters for PWE implementation

Lattice	Unit Cell Area	Resonators/Cell	Key FIBZ Points
Square	a^2	1	$\Gamma(0, 0), X(\pi/a, 0), M(\pi/a, \pi/a)$
Rectangular	$a_x a_y$	1	$\Gamma(0, 0), X(\pi/a_x, 0), M(\pi/a_x, \pi/a_y)$
Triangular	$a^2 \sqrt{3}/2$	1	$\Gamma(0, 0), X(4\pi/3a, 0), M(\pi/a, \pi/(a\sqrt{3}))$
Honeycomb	$3a^2 \sqrt{3}/2$	2	$\Gamma(0, 0), X(4\pi/(3a\sqrt{3}), 0), M(\pi/(a\sqrt{3}), \pi/(3a))$
Kagomé	$2a^2 \sqrt{3}$	3	$\Gamma(0, 0), X(2\pi/(3a), 0), M(\pi/(2a), \pi/(2a\sqrt{3}))$

1214 **Appendix B. EPWE Matrix Formulation for Complex Wave Vector
1215 Analysis**

1216 This appendix details the Extended PWE (EPWE) matrix formulation for com-
1217 puting complex wave vectors $k(\omega)$ at prescribed frequencies. The method solves
1218 the inverse eigenvalue problem, enabling direct analysis of wave attenuation and
1219 evanescent modes within bandgaps.

1220 Starting from the same governing equation (Eq. ??), EPWE maintains the Bloch
1221 expansion but reformulates the problem as a polynomial eigenvalue equation in
1222 k . The displacement field retains the form $w(\mathbf{r}) = \sum_{\mathbf{G}} w(\mathbf{G})e^{i(\mathbf{k}+\mathbf{G}) \cdot \mathbf{r}}$ where
1223 $\mathbf{k} = k_r + ik_i \in \mathbb{C}$ allows exponentially decaying modes.

1224 For wave propagation direction $\mathbf{k} = k(\cos \phi, \sin \phi)$, the governing equation yields
1225 a quartic polynomial eigenvalue problem:

$$[\mathbf{A}_3 k^3 + \mathbf{A}_2 k^2 + \mathbf{A}_1 k + \mathbf{A}_0] \psi = \mathbf{0} \quad (\text{B.1})$$

1226 where coefficient matrices depend on lattice geometry, frequency, and resonator
1227 coupling.

1228 The coefficient matrices for each reciprocal vector \mathbf{G}_i are constructed as:

$$\mathbf{A}_0[i, i] = \frac{DS}{a^4} |\mathbf{G}_i|^4 - \rho h S \omega^2 + D_j(\omega) \quad (\text{B.2})$$

$$\mathbf{A}_1[i, i] = \frac{4DS}{a^4} |\mathbf{G}_i|^2 (\mathbf{G}_i \cdot \hat{\mathbf{k}}) \quad (\text{B.3})$$

$$\mathbf{A}_2[i, i] = \frac{2DS}{a^4} [|\mathbf{G}_i|^2 + 2(\mathbf{G}_i \cdot \hat{\mathbf{k}})^2] \quad (\text{B.4})$$

$$\mathbf{A}_3[i, i] = \frac{4DS}{a^4} (\mathbf{G}_i \cdot \hat{\mathbf{k}}) \quad (\text{B.5})$$

1229 where $\hat{\mathbf{k}} = (\cos \phi, \sin \phi)$ is the propagation direction and $D_j(\omega) = k_j^* - (k_j^*)^2 / (k_j^* -$
1230 $\omega^2 m_{r,j})$ is the frequency-dependent dynamic stiffness from Eq. ??.

1231 Companion matrix linearization transforms Eq. ?? into the generalized eigen-

1232 value problem:

$$\begin{bmatrix} -\mathbf{A}_3 & -\mathbf{A}_2 & -\mathbf{A}_1 & -\mathbf{A}_0 \\ \mathbf{I} & \mathbf{0} & \mathbf{0} & \mathbf{0} \\ \mathbf{0} & \mathbf{I} & \mathbf{0} & \mathbf{0} \\ \mathbf{0} & \mathbf{0} & \mathbf{I} & \mathbf{0} \end{bmatrix} \begin{bmatrix} \psi_1 \\ \psi_2 \\ \psi_3 \\ \psi_4 \end{bmatrix} = k \begin{bmatrix} \mathbf{I} & \mathbf{0} & \mathbf{0} & \mathbf{0} \\ \mathbf{0} & \mathbf{0} & \mathbf{0} & \mathbf{0} \\ \mathbf{0} & \mathbf{0} & \mathbf{0} & \mathbf{0} \\ \mathbf{0} & \mathbf{0} & \mathbf{0} & \mathbf{0} \end{bmatrix} \begin{bmatrix} \psi_1 \\ \psi_2 \\ \psi_3 \\ \psi_4 \end{bmatrix} \quad (\text{B.6})$$

1233 Computational algorithm: (1) For each frequency ω , compute coefficient matrices using Eqs. (??)-(??) with the same reciprocal vectors from Appendix A; (2)
1234 Assemble companion matrix Eq. (??) of size $4N_g \times 4N_g$ with $N_g = (2M + 1)^2$;
1235 (3) Solve eigenvalue problem to extract $4N_g$ complex wave vectors k_i ; (4) Apply
1236 eigenvector tracking for mode continuity across frequency; (5) Normalize results:
1237 $k_{\text{norm}} = k \cdot a / (2\pi)$.

1238 Physical interpretation: $\text{Re}(k)$ represents propagating modes while $\text{Im}(k) > 0$
1239 quantifies evanescent decay. The attenuation constant $\mu = \text{Im}(k) \cdot a$ [Np/cell]
1240 directly measures wave attenuation within bandgaps. Typical computational
1241 parameters: $M = 2 - 3$ plane waves provide convergence for EPWE due to
1242 polynomial scaling, with frequency resolution $\Delta f = 1 - 10$ [Hz] depending on
1243 application requirements.
1244

1245 Appendix C. Framework for Lattice Selection in Engineering Applications

1247 The individual analyses presented in Section ?? reveal distinct performance
1248 characteristics that enable systematic lattice selection based on application re-
1249 quirements. This appendix synthesizes the comparative findings into practical
1250 engineering guidelines through performance metrics, design trade-offs, and a
1251 quantitative decision framework.

Appendix C.1. Performance-Based Design Categories

1253 The five lattice geometries exhibit distinct optimization characteristics that de-
1254 fine three fundamental design categories:

Peak Performance Category (Kagomé): Maximizes absolute attenuation through multi-resonator coupling, achieving -292.65 [dB] with highest material utilization ($m_{ratio} = 1.00$). Optimal for applications requiring maximum vibration suppression at specific target frequencies with material efficiency as secondary consideration.

1260 Balanced Performance Category (Honeycomb, Square): Provides moderate-
1261 to-high attenuation with predictable frequency response. Honeycomb (-220.33
1262 [dB]) offers dual-mode capability for frequency-selective applications, while square
1263 (-173.09 [dB]) delivers consistent single-mode performance for standard vibra-
1264 tion control requirements.

1265 Broadband Category (Triangular): Optimizes bandwidth-to-performance
1266 ratio with exceptional area efficiency. Despite minimal material usage ($m_{ratio} =$
1267 0.25), achieves near-peak performance (-174.19 [dB]) with superior FBGW char-
1268 acteristics (≈ 150 [Hz]), ideal for applications requiring robust performance
1269 across wide frequency ranges.

1270 Specialized Applications (Rectangular): Limited performance (-129.93 dB) compensated by geometric anisotropy enabling directional wave control

¹²⁷² and space-constrained implementations where unit cell aspect ratio is predeter-
¹²⁷³ mined by structural constraints.

¹²⁷⁴ *Appendix C.2. Quantitative Selection Framework*

¹²⁷⁵ Based on the comparative analysis, Table ?? presents a quantitative decision
¹²⁷⁶ matrix correlating application requirements with optimal lattice configurations:

Table C.19: Quantitative framework for lattice selection in engineering applications. Performance Score (*): Weighted average (peak attenuation 40%, bandwidth 30%, material efficiency 20%, manufacturing feasibility 10%). Abbreviations: Att. = Attenuation; Mat. Eff. = Material Efficiency; Perf. = Performance; Manuf. = Manufacturing; App. = Applications; Opt. = Optimal; Freq. = Frequency.

Criterion	Kagomé	Honeycomb	Triangular	Square	Rectangular
<i>Performance Metrics</i>					
Peak Att. [dB]	-292.65	-220.33	-174.19	-173.09	-129.93
Mat. Eff. Rank	1st	2nd	5th	3rd	4th
Bandwidth Perf.	Narrow	Dual-mode	Excellent	Moderate	Limited
Freq. Selectivity	High	Medium	Low	Medium	Medium
<i>Application Characteristics</i>					
Manuf. Complex.	High	Medium	Low	Low	Low
Target App.	Max supp.	Dual flex.	Broadband	Standard	Direction.
Opt. Freq. [Hz]	10-30	10-50	30-150	30-100	30-80
<i>Overall Assessment</i>					
Perf. Score*	10.0	8.5	9.2	7.8	5.9

¹²⁷⁷ *Appendix C.3. Application-Specific Design Guidelines*

¹²⁷⁸ The framework establishes four primary application scenarios with correspond-
¹²⁷⁹ ing optimal lattice selection:

¹²⁸⁰ **Scenario 1 - Critical Vibration Isolation:** Applications requiring maxi-
¹²⁸¹ mum attenuation at specific frequencies (precision instrumentation, sensitive
¹²⁸² equipment mounting). *Recommended:* Kagomé lattice for peak performance,
¹²⁸³ honeycomb as secondary option with manufacturing advantages.

1284 **Scenario 2 - Broadband Noise Control:** Systems operating across wide
1285 frequency ranges (automotive panels, building facades, aerospace structures).
1286 *Recommended:* Triangular lattice for optimal bandwidth-performance balance,
1287 square lattice for standard requirements.

1288 **Scenario 3 - Multi-Frequency Applications:** Environments with distinct
1289 frequency components requiring selective attenuation (industrial machinery, HVAC
1290 systems). *Recommended:* Honeycomb lattice for dual-mode capability, kagomé
1291 for primary frequency with secondary suppression.

1292 **Scenario 4 - Constrained Design Space:** Applications with predetermined
1293 geometric constraints or directional requirements (architectural integration, retrofit
1294 applications). *Recommended:* Rectangular lattice for anisotropic control, square
1295 lattice for space-efficient implementation.

1296 This framework transforms lattice selection from empirical approaches to system-
1297 atic engineering decision-making, enabling optimal configuration choice based
1298 on quantifiable performance metrics and application-specific requirements. The
1299 decision table provides engineers with concrete guidelines derived from the com-
1300 prehensive comparative analysis presented in Sections ?? and ??, establishing
1301 a bridge between theoretical insights and practical metamaterial design.